Chapter 1

Introduction

1.1 Motivation

The rapid technology evolution of Si MOSFET is beneficial for IC design with higher device speed and cost reduction. Besides the advantages on digital performance, the scaling of CMOS technology has largely improved the RF performance of MOS devices. The most significant improvement along with CMOS technology scaling is the larger RF gain, higher cut-off frequency (f_t) and maximum oscillation frequency (f_{max}) [1]-[11]. This has made CMOS device technology the prime choice for Mixed-Signal/RF system-on-chip (SoC) application such as WCDMA, W-LAN, and Ultra-Wide Band (UWB) wireless communication. The single chip radio design requires integration of high-performance analog components for base-band signal processing, high-performance RF transistors and passive components for low noise amplifiers and mixers, and high voltage components for power management. These elements are necessary to realize a single-chip RF transceiver design.

Among the passive components for mixed-signal and radio-frequency design application, Metal-Insulator-Metal (MiM) capacitors are the most important passive components. The process design of MiM materials and structures is much more difficult after Cu was introduced into the BEOL process technology. The choice of MiM materials will significantly influence the performance of MiM capacitors. We have therefore compared the performance and process complexity by using different materials as the electro-plates and insulator dielectric of the MiM capacitors. The process issues while integrating the MiM capacitor into the Cu BEOL are also discussed. Our results showed that the MiM performance can be optimized by properly optimizing the MiM process

conditions to achieve both high performance and reliable MiM capacitor integrated in the Cu BEOL.

The scaling on CMOS technology has improved device speed and reduced cost per transistor. The maximum oscillation frequency (f_{max}) is also improved larger than 40 GHz for 0.18 μm technology node [1]. The implementation of Cu interconnect in 0.13 μm technology significantly reduces the wire resistance and improves the quality factor of passive components. However, the low drain breakdown voltage of CMOS transistors limits the usage of CMOS for power amplifiers. This limitation for high voltage operation significantly reduces the maximum output power and efficiency for CMOS devices. Therefore, the RF SoC design, which includes the RF power amplifier, is a long time historical challenge for using the baseline CMOS logic process. In the past, the LDMOS transistors were introduced to overcome the low drain break-down voltage issue at the expense of complex process and lower operation speed [12]-[14]. However, this is opposite to the technology trend for wireless communication, where continuously increasing operation frequency is needed. To overcome the low breakdown voltage issue and improve the RF power performance, we designed an asymmetric lightly-doped-drain (LDD) MOS transistor for high frequency RF power application. This new asymmetric-LDD MOS transistor is fully embedded in the conventional foundry logic process without any additional process step or extra cost. The drain breakdown voltage at V_{gs}=0 V (BV_{dss}) is increased from 3.6 V in conventional transistor to 7.0 V in this new asymmetric-LDD device for the same 0.23 μm gate length. By properly increasing the drain operation point at 2.5 V for the new asymmetric-LDD MOS transistor, the output power can be increased to 38% at 2.4 GHz under peak power-added efficiency (PAE) condition.

The efforts to integrate high-quality MiM capacitor into Cu-BEOL and design a

new high-efficiency power MOSFET for low-voltage power amplifier application is a step further to realize the MS/RF SoC design.

1.2 Outline of the Dissertation

The single chip transceiver design requires integration of high-performance analog components for base-band signal processing, high-performance RF transistors and passive components for low noise amplifiers and mixers, and high voltage components for power management. In my research, it includes three parts to cover the importance topics on realizing the RF-SoC design in Si-MOS process technology. The first part is RF noise optimization and modeling. The research is to provide guidance for performance optimization on LNA design. The second part is MiM integration with Cu-BEOL process. This is to discuss the issues of this key passive component while being integrated into Cu-BEOL process for analog/mixed-signal design. The third part is the improvement of RF power performance on Si-MOS transistor by a new device structure. This part is to address the difficult topic of integrating Si-MOS power amplifier into RF-SoC design. Therefore, my research is to discuss the device and process issues we faced while realizing a single-chip transceiver design.

In this dissertation, we started with the introduction of basic RF parameter definition, power measurement method, and RF noise optimization and modeling for RF system in Chapter 2.

In Chapter 3, we discussed the process design consideration and performance comparison of different materials as the bottom electro-plat of MiM capacitors. The difficulty of integrating the MiM capacitor into the Cu BEOL is also discussed. We have also discussed how to improve the breakdown voltage (V_{bd}) failure of the MiM capacitor. Different insulator dielectrics have different electrical characteristics. We have compared

the electrical characteristics of MiM capacitors by using Si_3N_4 and SiO_2 dielectrics as the insulator dielectrics.

In Chapter 4, we introduce a new asymmetric-LDD MOSFET for low-voltage power amplifier application with high speed. The asymmetric-LDD MOSFET is a new design which is fully-embedded in the conventional logic process without any added process step and cost. The device design, layout, and how to realize this new asymmetric-LDD transistor is explained. We have also compared the DC and RF power performance between the conventional MOSFET and the new asymmetric-LDD transistor.

We conclude our research results in Chapter 5. The opportunities and future works are also discussed.

Chapter 2

Basic Parameter Definition and RF Noise

This chapter introduces the definition of important RF parameters and RF noise. RF noise is important for low-noise-amplifier (LNA) since the noise from the MOSFET of first stage LNA will dominate the noise floor of the whole communication system. We have studied how to optimize RF performance by properly select finger width and finger number at a fixed total finger width. The accurate RF noise modeling of the nm-scale MOSFETs is challenging due to the limited understanding of noise sources and the large parasitic effect from low resistivity Si substrate. We have established an equivalent circuit model with intrinsic BSIM3 model, connected gate resistance, through transmission lines and probing pads to get the intrinsic RF noise of MOS device.

2.1 Basic RF Parameters

The basic RF parameters to be discussed in this dissertation include Q-factor, cut-off frequency (f_t), maximum oscillation frequency (f_{max}), and Power-Added-Effiency (PAE).

The quality factor (Q-factor) for a system under sinusoidal excitation at a frequency ω can be defined by the following equation [15]

$$Q \equiv \omega \frac{\text{energy stored}}{\text{average power dissipated}} \tag{2.1}$$

For a parallel RLC network at resonance, $Q = \omega_0 RC$ where ω_0 is the resonant frequency of the RLC network.

At radio-frequency range, a two-port network can be adequately characterized by the scattering parameters (S-parameters). The S-parameters exploit the fact that a line

terminated in its characteristic impedance gives rise to no reflections. Scattering parameters define the input and output variables in terms of incident and scattered voltage waves. Figure 2.1 illustrates a two-port network wit the definitions of S-parameter port variables. The source and load terminations are Z_0. The two-port relations may be written as

$$b_1 = s_{11}a_1 + s_{12}a_2 \tag{2.2}$$

$$b_2 = s_{21}a_1 + s_{22}a_2 \tag{2.3}$$

where

$$a_1 = E_{i1} / \sqrt{Z_0} \tag{2.4}$$

$$a_2 = E_{i2} / \sqrt{Z_0} \tag{2.5}$$

$$b_1 = E_{r1} / \sqrt{Z_0} \tag{2.6}$$

$$b_2 = E_{r2} / \sqrt{Z_0} \tag{2.7}$$

The short-circuit current gain (H_{21}) and the maximum available gain (MAG) can be calculated by the following equations [16]

$$H_{21} = \frac{-S_{21}}{(1-S_{11})(1+S_{22})+S_{12}S_{21}} \tag{2.8}$$

$$MAG = k\left|\frac{S_{21}}{S_{12}}\right| - \sqrt{k^2-1} \tag{2.9}$$

where k is the stability factor and defined by

$$k = \frac{1-|S_{11}|^2-|S_{22}|^2+|S_{11}S_{22}-S_{12}S_{21}|^2}{2|S_{12}||S_{21}|} \tag{2.10}$$

There are two important characteristic frequencies which indicate the high frequency capability of the transistors. The cut-off frequency (f_t) is the frequency when the short-circuit current gain H_{21} of the device is equal to unity. The maximum oscillation

frequency f_{max} is defined as the frequency at which the MAG is equal to unity.

2.2 RF Power Measurement

The RF power characterization was carried out by on-wafer measurements using an ATN load-pull system, where the input and output impedance matching conditions were selected to optimize the output power.

The power added efficiency (PAE) of the power amplifier is used to indicate the power drawn from the supply and is defined as

$$PAE = \frac{(P_{rf,out} - P_{rf,in})}{P_{dc}} \tag{2.11}$$

where $P_{rf,out}$ is the RF output power, $P_{rf,in}$ is the RF input power, and P_{dc} is the total dc power drawn from the power supply.

2.3 RF Performance Dependence on Layout

By scaling down the gate length, the unity-current-gain frequency (f_t) can be increased to ~120 GHz in 0.13 μm low-voltage logic process with 80 nm physical channel length as shown in Fig. 2.2. The fast f_t has made CMOS a popular choice for RF system-on-chip (SoC) up to tenth GHz for wireless communication. In additional to high f_t, the RF Noise is the other important parameter to consider while scaling down the MOSFETs. The noise from the MOSFET of first stage low-noise amplifier (LNA) will dominate the noise floor of the whole communication system. We have studied the dependence of minimum noise figure with finger number and finger width at a fixed total finger width. The CMOS processes provided to designers are usually fixed and difficult for designer to change the transistor performance. However, there is still a way for designers

to optimize the performance of cut-off frequency, minimum noise figure, and associated gain based on the design requirement. By properly choosing the finger number and finger width, the designers can still optimize the RF performance and better fit the system requirement.

Fig. 2.3 shows the measured NF_{min} and associated gain at 10 GHz of MOSFETs fabricated by 0.18 μm and 0.13 μm technologies. The NF_{min} decreases monotonically with increasing gate finger numbers that is due to the decreasing gate resistance in parallel and hence the reduced thermal noise. A reducing NF_{min} of 0.3 dB to 1.0 dB is obtained in n-MOSFETs as scaling down from 0.18 μm node to 0.13 μm. Among various layout of different finger numbers and finger width, a lowest NF_{min} of 0.87 dB is measured at 10 GHz in 0.13 μm MOSFET with 72 fingers and 4 μm width that is comparable with the best reported RF noise data of MOSFETs. In addition, high associated gain from 15 to 20 dB is measured that is desirable for amplifier design. Another merit of this 0.13 μm MOSFET is that the high associated gain (~20 dB), low NF_{min} (1.0 dB) and small power consumption can be simultaneously achieved at 0.13 μm MOSFET with lowest 6 fingers suggests the excellent RF device performance. In contrast to large noise improvement, the small associated gain increase in MOSFETs as scaling down from 0.18 μm to 0.13 μm is due to the reverse feedback capacitance C_{gd}. This is because the associated gain is proportional to gm/C_{gd}, but the scaling down usually gives poor C_{gd} related reverse feedback S_{12}.

As mentioned earlier, the measured NF_{min} is also strongly dependent on finger width. To understand such finger width dependence, we have first compared the transistor RF performance by measuring the f_t. Fig. 2.4 shows the measured f_t as a function of finger width. For the same total gate width of 72 μm by multiplying the gate fingers and finger width, the peak f_t increases with increasing finger width because the total parasitic capacitance due to Shallow-Trench-Isolation (STI) corner is reduced by increasing finger

width.

Fig. 2.5 shows the measured associated gain at 10 GHz by varying the finger width under the constant total gate width of 72 μm. The decreasing associated gain is due to the increased gate resistance with increasing channel width under the constant total gate width condition. The optimization of f_t, NF_{min}, and associated gain can be done through finger width and finger number adjustment under a constant total finger width.

The downscaling evolution of Si MOSFETs can achieve better RF performance on unit-current-gain cutoff frequency (f_t), the minimum noise figure (NF_{min}), and associated gain. The NF_{min} has also a strong dependence on channel width and finger number. The RF noise can be optimized through a proper choice of RF device layout.

2.4 RF Noise Modeling

The increasing operation frequency to higher band with wider bandwidth is the technology trend for communication system. The demand of high-performance low noise MOSFET becomes more urgent for ultra-wide band (UWB) (3.1-10.6 GHz) beyond current W-LAN (5.2-5.8 GHz), since the noise also increases monotonically with increasing frequency. However, accurate RF noise modeling of the nm-scale MOSFETs is challenging due to the limited understanding of noise sources and the large parasitic effect from low resistivity Si substrate. Another problem for the nm-scale MOSFET is the large gate resistance where a parallel multiple gate fingers layout is used to reduce the R_g generated thermal noise. Unfortunately, the consumed DC and RF power also increase with increasing finger number that is contradictory to the low power trend. In this paper, we have modeled and analyzed the minimum noise figure (NF_{min}) of multi-fingers 0.13 μm node MOSFETs (~80 nm physical gate length) using low-voltage logic process. In contrast to the as-measured large NF_{min} value and strong dependence on parallel fingers, the

de-embedded intrinsic NF_{min} has much smaller noise value and weak dependence on gate fingers. From measured data and circuit analysis, the large as-measured NF_{min} is due to the small impedance of large probing (substrate loss) that dominating the measured noise.

Multiple gate-fingers layout is used to reduce the gate resistance (8 Ω/sq) of 0.13 μm node MOSFETs (LG ~80 nm) by connecting them in parallel. Large gate fingers from 6, 18 to 36 are studied but the drain current also increases from 11, 28 to 57 mA. Further increasing gate finger beyond 36 is limited by the large power consumption. The S-parameters are measured from 300 MHz to 30 GHz using network analyzer. The $NF_{\min}$ and associated gain are measured using ATN-NP5B Noise Parameter Extraction System up to 10 GHz and useful for UWB. The conventional way to de-embed $NF_{\min}$ requires removing parasitic open and through lines effects from as-measured $NF_{\min}$ by using series matrix calculations. In this work, we have used the same ideal but the equivalent circuit model to de-embed the measured $NF_{\min}$. This method can give not only the de-embedded $NF_{\min}$ but also additional information of noise source analysis beyond conventional method. As shown in Fig. 2.6, the un-de-embedded noise model includes the MOSFET, through lines and probing pads at both I/O ports. The BSIM3 model parameters of MOSFET in Fig. 2.6 are obtained by standard extraction procedure. To reduce the through line effect, the layout of very short and thin transmission line, shown in Fig. 2.7, is used to largely reduce the thermal noise from series R_{thru} and shunt R_{sub} of through line. This is justified from the contributed DC resistance of only ~0.2 Ω from the through line.

Since the measured noise includes the large probing pad effect, we have first simulated the as-measured S-parameters with pad. Figs. 2.8(a) and 2.8(b) show the as-measured and modeled S-parameters for the smallest 6 and largest 36 fingers 80 nm MOSFETs, respectively. Good agreement between measured and modeled S-parameters is obtained suggesting the good accuracy of circuit model in Fig. 2.6, where the equivalent

circuit model for open pad in I/O ports is from the well matched simulation of open pad sub-circuit with measured S-parameters.

Figs. 2.9(a) and 2.9(b) show the as-measured and simulated $NF_{\min}$ of the smallest 6 and largest 36 fingers 80 nm MOSFETs, respectively, where the simulated data is from the equivalent circuit model in Fig. 2.6 with extrinsic modeling parameters from the well matched S-parameters in Fig. 2.8. The excellent agreement between as-measured and simulated $NF_{\min}$, in combining with the well matched S-parameters in Fig. 2.8, indicates the good accuracy of circuit model in Fig. 2.6. Therefore, the same model is suitable to provide self-consistent solutions for $NF_{\min}$, S-parameters, and DC (from extracted BSIM3 modeling parameters).

We have further used the well matched equivalent circuit model to de-embed the noise generated from the probing pad. The pad equivalent sub-circuit is included inside the extrinsic model in Fig. 2.6 and the parameters values are obtained from the well agreed simulation data with measured S-parameters of open pad. The de-embedded $NF_{\min}$, is also shown in Fig. 2.9, which is largely reduced from as-measured data to only 1.1-1.2 dB at 10 GHz for both fingers MOSFETs. This suggests that the probing pad contributes the dominant noise source in as-measured $NF_{\min}$, because of its low impedance shunt pass connected to gate, where such effect can be greatly reduced by increasing substrate resistivity.

To further understand such large contribution of probing pad, we have analyzed the excess noise generated by both pad and gate resistance. Fig. 2.10(a) shows the typical noise circuit of MOSFETs with two equivalent input noise generators. However, this simplified noise circuit did not consider the thermal noise from both gate resistance and shunt pass resistance of probing pad. Fig. 2.10(b) shows the modified noise circuit including the R_g and R_{pad} thermal noise sources. To include these additional thermal noises

and translate into the two equivalent input noise generators in Fig. 2.10(a), short and open circuiting the input are required. The reason why open pad R_{pad} generates dominant noise is due to the formation series or parallel connection with R_g during open or short circuiting. Since the R_{pad} is larger than R_g even at the smallest 6 finger devices, its generated thermal noise becomes the dominant factor in NF_{min}.

We have shown that the dominant noise source is from the probing pad generated thermal noise, which is due to the lossy Si substrate effect. The NF_{min} is largely reduced from the as-measured 3-6 dB to only small 1.1-1.2 dB after de-embedding for 6, 18 and 36 fingers 80 nm MOSFETs. The weak dependence of NF_{min} after de-embedding is due to the combined effect of $R_g g_m$ and nearly constant where the increasing finger number decreases R_g but also increases g_m monotonically.

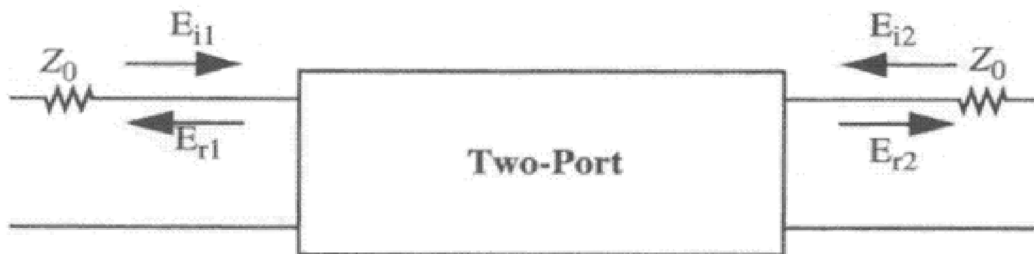

Fig. 2.1 Two-port network

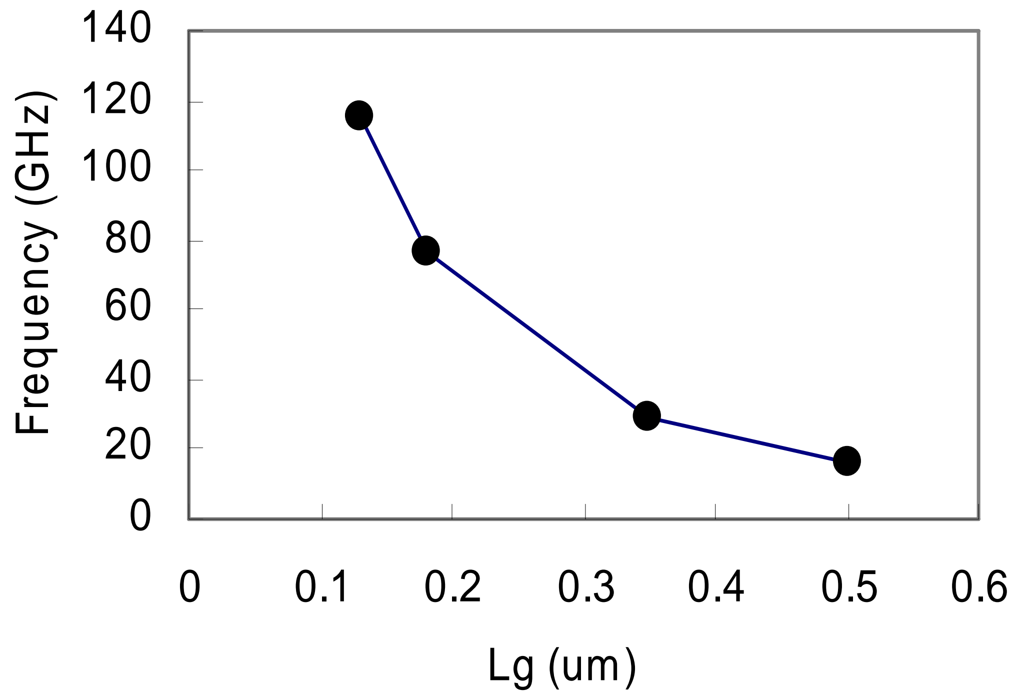

Fig. 2.2 The dependence of cut-off frequency f_t on scaling down the L_g. f_t is increased to >100 GHz with 4 μm channel width and a finger number of 18 at 0.13 μm technology node.

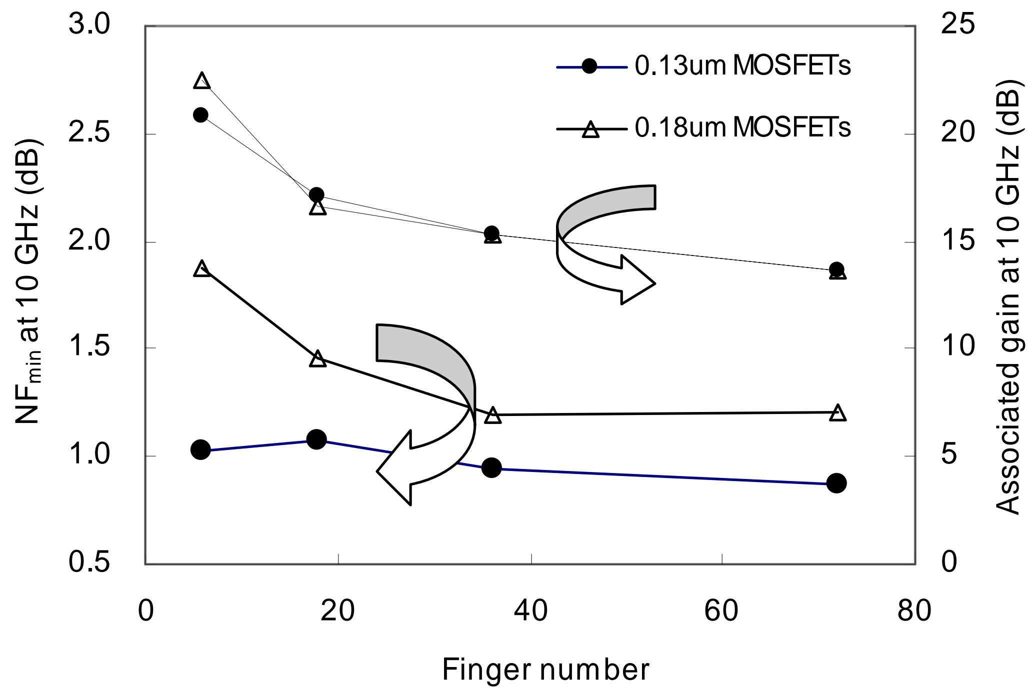

Fig. 2.3 The measured NF_{min} and associated gain at 10 GHz of n-MOSFETs using 0.13 μm and 0.18 μm technology. The channel width is 4 μm and multi-fingered device layout is used to reduce the gate resistance.

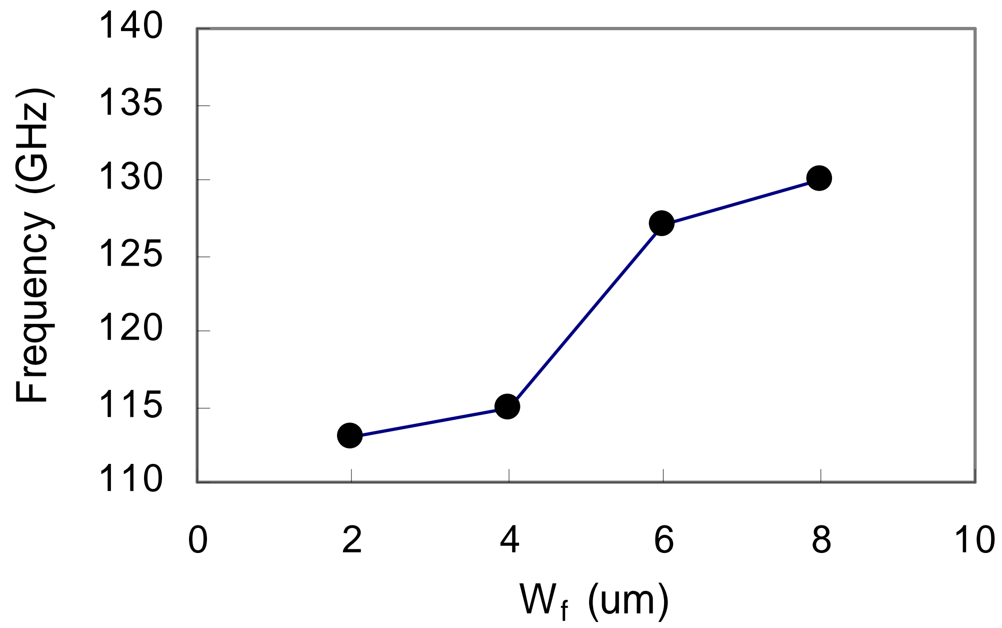

Fig. 2.4 The dependence of f_t on finger width under a fixed total gate width of 72 μm. The f_t increases to 130 GHz with 8 μm finger width and a finger number of 9 for 0.13 um technology node.

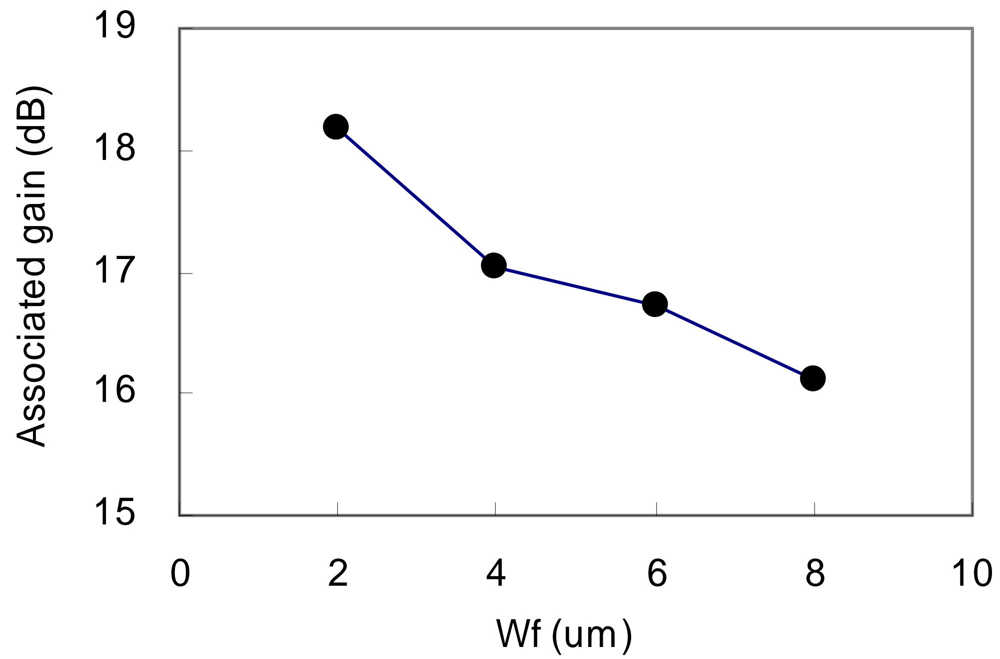

Fig. 2.5 The dependence of associated gain on finger width under a fixed total gate width of 72 μm. The associated gain decreases monotonically with increasing finger width.

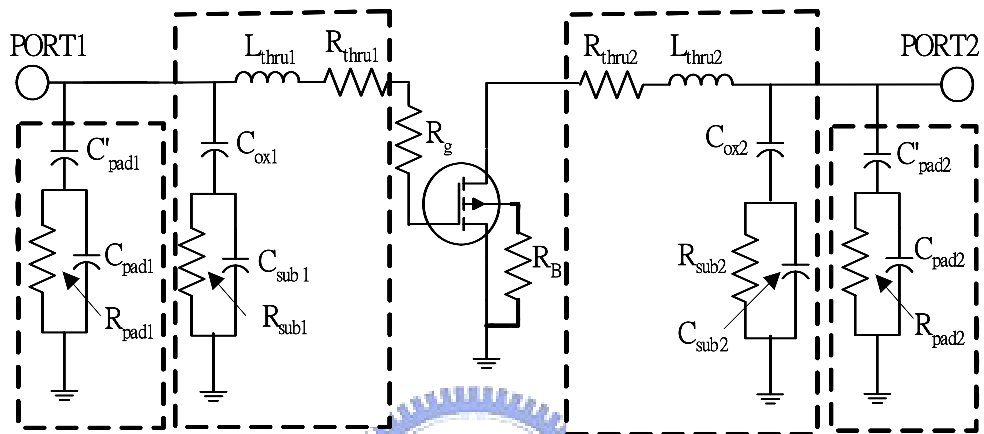

Fig. 2.6 The extrinsic equivalent circuit model for RF MOSFET that contains intrinsic BSIM3 MOSFET model, connected gate resistance R_g, through transmission lines and probing pads. The shunt impedance to ground from through line is much larger than probing pad due to the short and thin line layout.

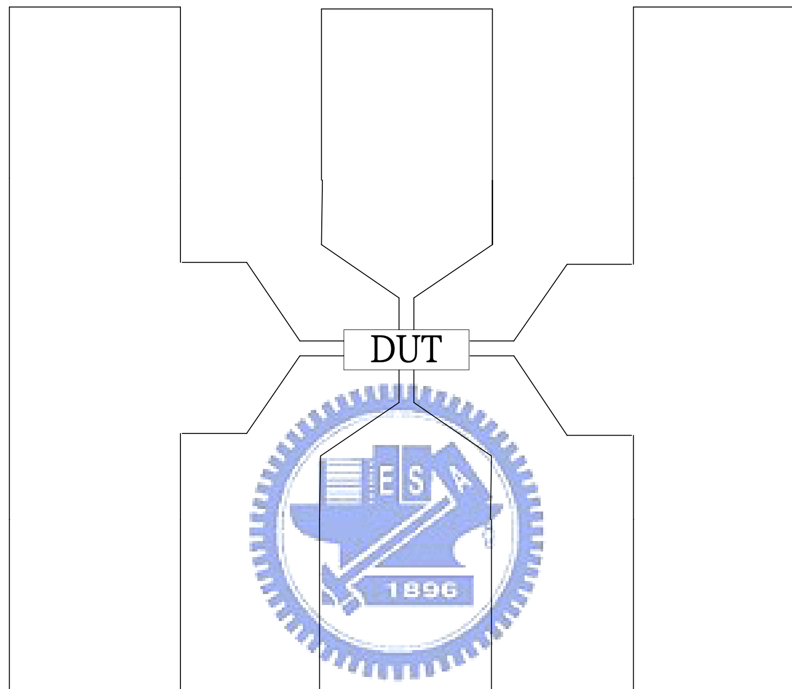

Fig. 2.7 The schematic diagram of probing pad and through transmission line connected to device under test. Short and thin through line is used to reduce its noise generation.

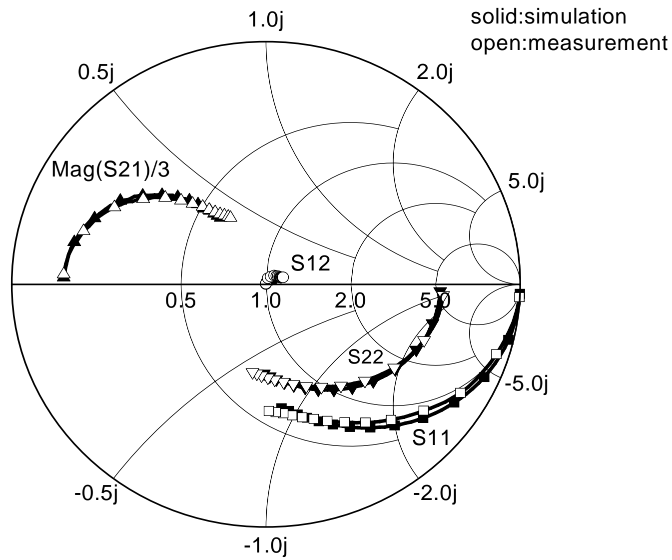

(a)

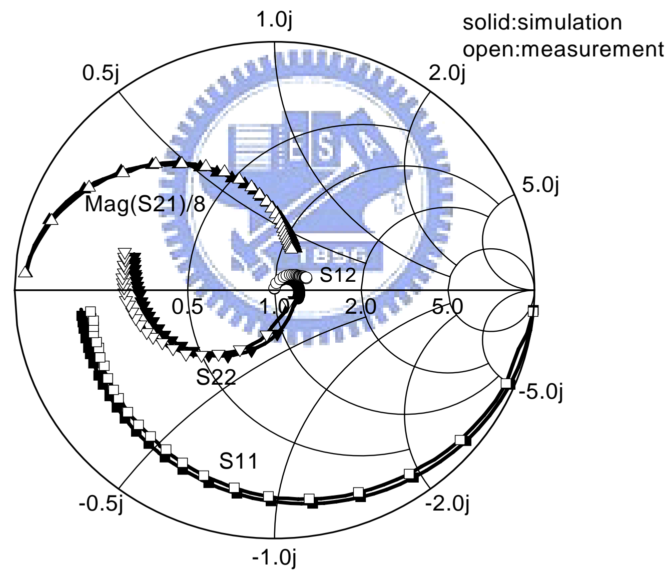

(b)

Fig. 2.8 The as-measured and modeled S-parameters of 80 nm MOSFETs with probing pad for (a) the smallest 6 and (b) the largest 36 gate fingers. The good agreement indicates the good accuracy of model in Fig. 2.6. The S_{21} is divided by respective 3 or 8 to fit in the unity radius Smith Chart due to the large gain.

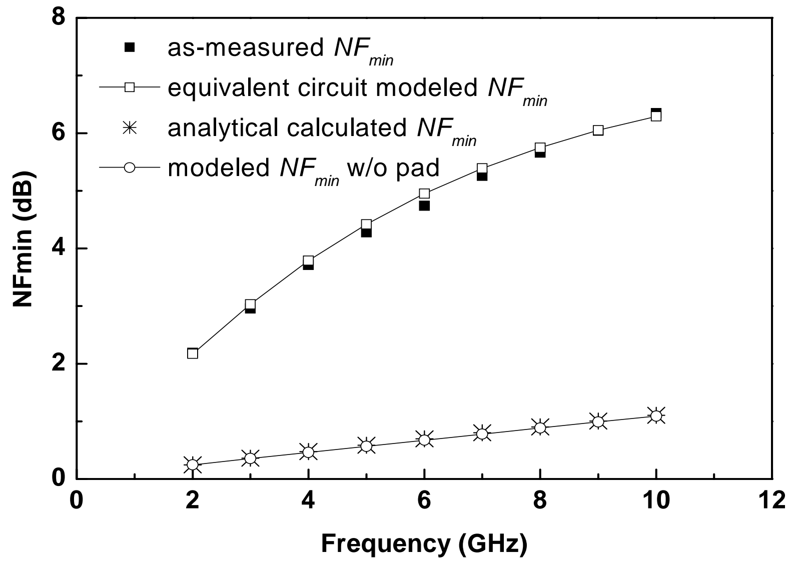

(a)

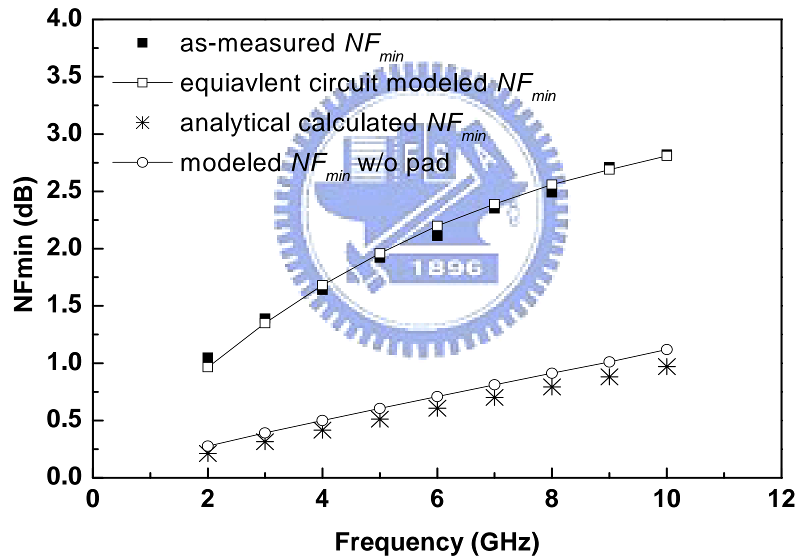

(b)

Fig. 2.9 The measured and modeled $NF_{\min}$ of 80 nm MOSFETs with (a) the smallest 6 and (b) the largest 36 fingers. The good agreement between as-measured and simulated $NF_{\min}$ indicates the good accuracy of model in Fig. 2.6. The probing pad shows the dominant effect on as-measured $NF_{\min}$. The analytical calculation is also added for comparison.

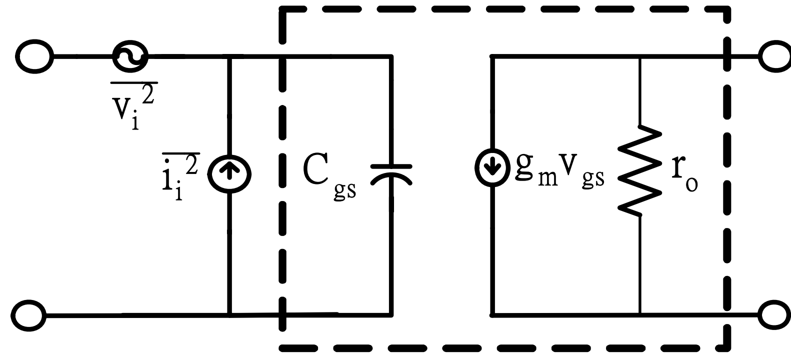

(a)

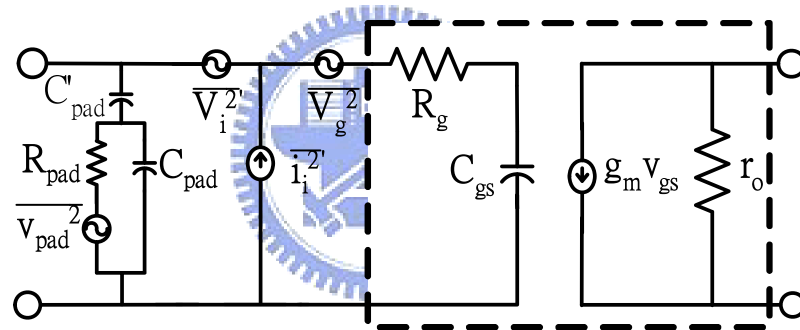

(b)

Fig. 2.10 The noise circuit of MOSFETs with (a) simplified two equivalent input noise generators and (b) our proposed model with additional noises from R_g and R_{pad}. To convert our proposed noise circuit in (b) into two equivalent input noise generators case in (a), open and short circuiting are required.

Chapter 3

Process Design and Considerations of Metal-Insulator–Metal Capacitors

The improved high-frequency performance of CMOS devices after technology scaling has led to more product designs with integrated mixed-signal/RF elements into CMOS process. This chapter starts with the discussion of active/passive elements necessary for mixed-signal/RF process and followed by the discussion of process concerns while implementing MiM (metal-insulator-metal) capacitors into Cu-BEOL (Back-end-of-Line) process.

3.1 Overview of Mixed-Signal/RF Components

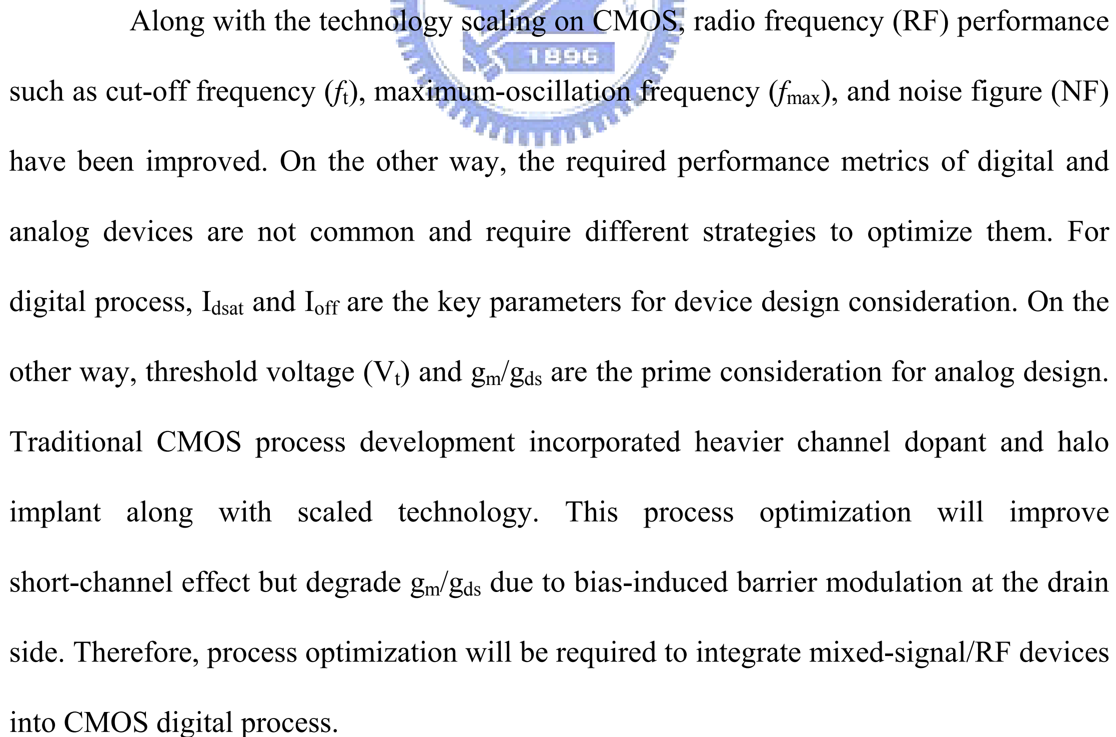

Along with the technology scaling on CMOS, radio frequency (RF) performance such as cut-off frequency (f_t), maximum-oscillation frequency (f_{max}), and noise figure (NF) have been improved. On the other way, the required performance metrics of digital and analog devices are not common and require different strategies to optimize them. For digital process, I_{dsat} and I_{off} are the key parameters for device design consideration. On the other way, threshold voltage (V_t) and g_m/g_{ds} are the prime consideration for analog design. Traditional CMOS process development incorporated heavier channel dopant and halo implant along with scaled technology. This process optimization will improve short-channel effect but degrade g_m/g_{ds} due to bias-induced barrier modulation at the drain side. Therefore, process optimization will be required to integrate mixed-signal/RF devices into CMOS digital process.

The key difference between digital and mixed-signal process is the existence of

passive elements. The passive elements for mixed-signal/RF design includes FEOL (Front-end-of-Line) resistors, variable capacitors (varactors), vertical MiM capacitors, lateral BEOL (Back-end-of-line) line-to-line capacitors, and inductors. These passive components will limit the performance of mixed-signal/RF design. In mixed-signal/RF design, these passive components are designed to perform active functions such as filtering, tuning, gain control, and impedance matching. The performance of passive elements needs to be specially considered while developing the process.

There are three kinds of FEOL resistors; un-silicided polysilicon resistors, un-silicided diffusion resistors, and well resistors. Silicided resistors have much lower sheet resistance (5~15 ohm/sq) and are not adequate for resistors in mixed-signal/RF design. The design consideration on choosing FEOL resistors are sheet resistance, voltage coefficient, and temperature coefficient. The voltage and temperature coefficients are process-dependent (implant conditions, thermal cycle, and grain boundary size). Un-silicided resistors require an extra silicide-block module. However, process optimization for FEOL resistors are not specially considered in process development because the main focus is to optimize active devices. Certain Boolean operation might be applied on the resistor components to optimize the resistance targets. FEOL resistors will require proper modeling to be implemented into mixed-signal/RF design.

Inductors are critical components in mixed-signal/RF design. Inductors with small inductance and high-Q are employed in circuits such as RF transceivers. Larger inductors with low-Q are utilized for impedance matching and gain control. Inductors are usually implemented in the thicker upper layers of BEOL process to minimize resistance and inductive losses to the dissipative silicon substrate. To form an inductor, a minimum of two metal layers are required. One is to form the spiral and the other is to form the underpass. The layout and material of the inductors will directly impact the maximum

achievable Q-factor of the inductors. Lower serial resistance by thicker metal layer will improve the Q-factor at low frequencies and the inductive coupling to the substrate will limit the Q-factor at high frequencies. Proper layout optimization and substrate leakage path termination are key factors to improve the Q-factor of Inductors.

Precision/reference capacitors require tight matching and voltage/temperature linearity and stability. There are four major types of capacitors used in analog/mixed-signal design; polysilicon-insulator-polysilicon (PIP), metal-insulator-metal (MiM), lateral line-to-line and metal over metal stack (MoM), and MOS capacitors. Best performance is achieved by metal-insulator-metal (MiM) capacitors. MiM capacitors possess excellent linearity with voltage/temperature and matching performance. MiM capacitors are integrated near top of interconnect stack and require 1~2 additional mask steps to form the capacitor structures. In recent years, the increasing interest of analog/mixed-signal/RF processes has led to the implementation of MiM capacitors into Cu-damascene process beyond 0.13 μm technology. There are some issues with MiM capacitors while integrated with Cu-damascene process. The major concern is Cu metallurgy and its impact on yield and reliability. The choice of insulator and bottom/top electro-plates will affect the MiM performance. This chapter will discuss the process integration of MiM capacitors with Cu-damascene process beyond 0.13 μm process technology.

3.2 Process Concerns to Integrate MiM Capacitors into Cu BEOL

High quality passive elements integrated with logic have been the trend of MS/RF SoC. The on-chip integration of MiM capacitor and Inductors with logic process is

popular for area, cost, and performance enhancement. For 0.18 μm technology and beyond, aluminum is used as the logic interconnects. While integrating MiM with Logic process, one interconnect layer is usually used as the bottom electrode plate of MiM capacitors. The thick Al interconnect (~4 k) offers a low-resistance and planar electrode which results in a high-Q and low interface leakage. In the Cu back-end-of-line (BEOL) era, the use of Cu as the bottom electrode plate is the most cost-effective method since the Cu layer is also used for logic area without extra cost. Cu has also a very low resistivity and results in a high-Q performance. Our results showed that Cu can achieve Q~200 @2.4 GHz with 0.7 pF MiM capacitor. However, it had been reported that Cu roughness will cause MiM reliability problem [17]-[19]. In addition, Cu can be used for small area MiM but the performance will be significantly degraded for larger area MiM capacitors. Cu metallurgical roughness and Cu-CMP u-scratch are two factors for the worse early breakdown of MiM capacitors while Cu is used as bottom electrode plates. To develop highly reliable, high-Q, and high-yield MiM capacitors, we have compared different MiM bottom electrodes (Table 3.1), clarified the cause of reliability issue while using Cu as bottom electro-plates, and developed an optimized TaN/Al/TaN bottom electrode plate with highly reliable performance. The optimized method is to integrate TaN/Al/TaN into Cu-damascene process as the bottom electro-plate but keep the insulator dielectric and top electro-plate. The Q-value can achieve 115 @2.4 GHz with 0.7 pF MiM capacitor for TaN/Al/TaN bottom electro-plate. For pure TaN bottom electro-plate, the Q-factor is significantly degraded more than half due to high resistivity. For Al process, serious roughness was observed for thin Al layer. To resolve the field-enhancement due to roughness of thin Al as bottom electro plate, we had developed a method to optimize the process of aluminum deposition to fully resolve the roughness effect. A high-Q, highly reliable, and capable of manufacturing MiM process in

Cu-BEOL is realized.

The key factor on designing MiM capacitor is the unit capacitance. Silicon dioxide and silicon nitride are the usual insulator dielectrics of Metal-Insulator-Metal capacitors. Silicon dioxide has been widely used as dielectrics of MiM capacitors due to easy process integration with other materials and low leakage current. However, the dielectric constant of silicon dioxide is ~3.9 that is not suitable for MiM capacitors with high unit capacitance. As rule of thumb, MiM capacitors require silicon dioxide with thickness ~350 A as insulator dielectric to posses a unit-capacitance of 1 $fF/\mu m^2$. Lower cost processing requires much higher unit capacitance of MiM capacitors. The thickness of silicon dioxide needs to be significantly reduced by half to achieve a unit-capacitance of 2 $fF/\mu m^2$. The much higher leakage and reliability issues are the major concerns. To successfully increase unit capacitance without causing process and reliability issues, silicon nitride (Si_3N_4) are commonly used due to much higher dielectric constant (~7.5). There is higher leakage current (>10X) of MiM capacitors while using Si_3N_4 as the insulator dielectric. The higher leakage current needs to be taken into design consideration while using Si_3N_4 as the insulator dielectric of MiM capacitor. There are more researches studying on integration of high-*k* dielectrics (e.g. Ta_2O_5) into MiM capacitors to increase the unit capacitance significantly.

3.3 MiM Capacitor Process

The process discussed in this chapter was based on a 0.13 μm CMOS Mixed-Signal/RF process technology provided by IC foundry. There are two ways to integrate Meal-Insulator-Metal capacitors into Cu-damascene process. One way is to use Cu interconnect as the bottom electro-plate as shown in Figure 3.1. In this way, bottom electro-plate is defined at the same time as other circuit interconnects after Cu CMP. The

insulator dielectric and top electro-plate are subsequently deposited and a mask layer is required to define the top electro-plate. After top-electro-plate is defined, inter-metal-dielectric (IMD) is deposited. Top via layer is subsequently defined to connect top electro-plate and bottom electro-plate at the same time. The other way of realizing MiM capacitors is to insert MiM capacitors into the top two metal layers after processing the FEOL and Cu dual damascene process. For an eight layers of Cu interconnect, MiM capacitors are integrated into the BEOL process between seventh and eighth of Cu layer. The reason of inserting MiM capacitor to the top two metal layers is because top metal has larger process margin to cover the worse topography caused by MiM structure. By putting MiM capacitor between top two metal layers, the parasitic capacitance to the silicon substrate can also be reduced. The MiM structure is shown in Fig 3.2. After the 7th metal layer was patterned after Cu-CMP, an etching-stop layer was deposited for further processing. A thin TaN was deposited and sequentially followed by Aluminum and TaN deposition to form the bottom plate with TaN/AlCu/TaN film stack. Plasma-Enhanced-Chemical-Vapor-Deposition (PECVD) SiO_2 or Si_3N_4 was then deposited as the capacitor dielectric and followed by TaN deposition as top electro-plate. Two masks were used to pattern the top electro-plate and bottom electro-plate. After oxide deposition, via connection was formed to connect top-plate, bottom-plate, and Cu interconnect to the eighth layer of metal at the same time. The etching recipe of Via process needs to be optimized to properly land on bottom electro-plate and Cu interconnect but without etching through the top electro-plate. The oxide topography due to the stacked MiM structure is polished out by Cu-CMP while forming top metal interconnect. Therefore, the Cu interconnect thickness above the MiM structure will be much thinner (~MiM structure thickness) compared with the Cu interconnect without MiM capacitors beneath them. Due to the much thicker bottom electroplate of TaN/AlCu/TaN structure, the gap filling is a

challenge for process integration. One way to resolve this issue is to properly define the design rule and allow enough process marginality for gap filling between the MiM capacitors. Fig. 3.3 shows the TEM of integrated MiM capacitor with TaN/Al/TaN as bottom electrode-plate and TaN as top electrode-plate.

3.4 Performance Characterization of MiM Capacitors

In this section, we characterize MiM performance of various materials as bottom electrode-plate and insulator dielectrics. Q-factor, capacitance-voltage linearity, voltage-temperature linearity, leakage current vs. voltage, and MiM breakdown voltage are characterized and compared. The current-voltage (I-V), capacitance-voltage (C-V), and quality factor (Q-factor) were measured by HP4156, HP4284, and HP8510C, respectively.

For RF application, the quality factor of MiM capacitors with different bottom electrodes is shown on Figure 3.4. The quality factor can achieve ~200 for MiM capacitors with Cu as the bottom electroplate and Q~115 for TaN/Al/TaN electrodes at 2.4 GHz with 0.7 pF capacitance. For pure TaN bottom electroplate, Q factor can only achieve ~54 @2.4GHz due to higher resistivity. The capacitance increases at high frequency due to the resonance of parasitic inductor, which can be flat out by proper de-embedding procedure. From the Q-factor comparison among different materials as bottom electroplate, higher Q-factor can be achieved by lowering down resistance of bottom electroplate. By using Cu (also served as M7 for logic circuit) as bottom electroplate, the overall resistance reduction is maximized due to lower resistivity and thicker Cu for interconnect. However, the factor to influence the Q-factor of MiM capacitors is the series resistance along with this MiM structure including resistance at both terminals of the MiM capacitors. Therefore, it is favorable to put as many vias to connect top electroplate and bottom electroplate as possible.

In additional to high-Q, another important factor of MiM capacitors is the leakage current. This is especially important for high-density analog/RF ICs similar to the case in DRAM capacitors [20], [21]. In this research, we reduced the MiM leakage current by optimizing the MiM process. Typical leakage (J-V) behavior of different bottom electrode materials is shown in Figure 3.5. The asymmetric leakage with applied voltage is due to different surface roughness between top and bottom electrode-plates. For positive applied voltage at the top electro-plate, electrons are injected from the bottom-plate to top-plate. The roughness of the bottom electro-plate will be critical for creating sites with higher electric field. Under low electric field, the trap-assisted tunneling (TAT) of electrons from the electrode to trap states in the dielectric close to the electrode-dielectric interface will dominate the capacitor leakage [22]. Nitride dielectric showed a higher MiM leakage dependence with the applied voltage compared with Plasma-Enhanced Oxide (PEOX) dielectrics. This is caused by the intrinsic leakage characteristics of silicon nitride film. The leakage current is very low in the range of <1E-10 A/cm^2 at 1.2 V for optimized Al process condition with SiO_x. On the other way, the impact of asymmetric leakage due to different top and bottom electrode-plates is minor. The top electrode is deposited onto the dielectric material and there is no surface roughness issue. The top electroplate is also designed to connect the top metal line through via array and the resistance is much lower compared with bottom electrode plate. Therefore, the impact to MiM performance is minimal.

The comparison of MiM breakdown voltage (V_{bd}) performance is shown in Figure 3.6 with 1,000,000 um^2 MiM area for bottom electrode-plates with TaN and Al and 640,000 um^2 for bottom electrode-plate with Cu. The V_{bd} cumulative failure of Cu electrode-plate is much worse than TaN and TaN/Al/TaN electrodes due to worse surface roughness and inevitable Cu-CMP dishing. For small area MiM capacitors, Cu electrode is

still an option but high defect density will be a concern. For thin TaN/Al(<1.5 kA)/TaN electrode, the surface roughness is observed to be critical which was not significant for conventional Al(>3 kA)/TiN bottom electrode plate beyond 0.18 μm technology. By optimizing the process temperature and other process conditions of Al deposition process, the degradation of MiM V_{bd} by surface roughness is significantly reduced.

The reflectivity of TaN/Al/TaN electrode versus the waiting time of Al process also demonstrated robust process after optimization as shown in Figure 3.7. Before the process is optimized, the reflectivity will decrease significantly with process waiting time. For optimized thin Al process, the dependence with the waiting time of Al deposition process is negligible compared with original one. It indicates that the optimized Al deposition has a stable surface roughness with manufacturable process window.

Linearity is a critical characteristic for capacitors. Figure 3.8 shows the normalized capacitance of four different bottom electrode-plates versus temperature from 25 C to 125 C. Cu demonstrates minimal first-order temperature coefficient of capacitance with less than 40 ppm/^{o}C and ~30% reduction compared to that of TaN and TaN/Al/TaN. Figure 3.9 shows the normalized capacitance of three kinds of bottom electro-plates and two dielectric materials versus the bias voltage from –5 V to 5 V. TaN demonstrated much better first-order voltage coefficient of capacitance (VCC1) ~16 ppm/V compared with TaN/Al/TaN ~30 ppm/V. The second-order voltage coefficient of capacitance (VCC2) is comparable for different bottom electroplates. However, MiM dielectric with nitride has a positive VCC2 (22 ppm/V^2) compared to a negative VCC2 (-30 ppm/V^2) for SiO_x MiM dielectrics. The negative second-order voltage coefficient of capacitance for SiO_x dielectrics is due to the intrinsic leakage current while applying voltage. The positive VCC2 of silicon nitride film is due to charge trapping in the nitride film [23].

The development trend of MiM capacitor is to integrate high-k material to provide

a capacitor with high unit-area capacitance to minimize the chip area and reduce cost. The study of interface reaction between high-k and electrode materials needs to be carefully evaluated.

3.5 Summary

The incorporation of MiM capacitor into Cu-BEOL needs different approaches from Al-BEOL process technology. The adoption of process options depends on the intent of product design and MiM area. For high-Q and small MiM area product, Cu as a capacitor bottom plate is a suitable option but has a lower process yield. We think Cu as an bottom electro-plate is the best choice due to performance and simple process integration if the poor Vbd performance can be resolved by process optimization. TaN-based MiM capacitor can achieve low leakage and better linearity but a penalty of low quality factor ~54 @2.4 GHz due to higher resistivity. On the other way, a MiM capacitor with thin Al bottom plate can be achieved with optimized process condition. The Al-base MiM capacitor can achieve Q>100 at 2.4 GHz with ~0.7 pF capacitance. The optimized process conditions can achieve a very low defect density and suitable for manufacturing. The process design and performance comparison of integrating different MiM structures into Cu damascene process is discussed in this chapter.

Bottom Plate	**Cu**	**TaN**	**Thin Al**	**Optimized Al**	**Optimized Al**
Top Plate	TaN	TaN	TaN	TaN	TaN
Masks	1	2	2	2	2
Dielectric	SiOx	SiOx	SiOx	SiOx	Si_3N_4
C (fF/um^2)	1	1	1	1	2
Q @2.4GHz, 625um^2	~200	~54	~115	~115	
TCC (ppm/C)	-35 ppm/C	-50 ppm/C	-60 ppm/C	-50 ppm/C	
VCC1 (ppm/V)	30 ppm/V	16 ppm/V	30 ppm/V	30 ppm/V	55 ppm/V
VCC2 (ppm/V^2)	-30 ppm/V^2	-30 ppm/V^2	-33 ppm/V^2	-30 ppm/V^2	22 ppm/V^2
Mis-Matching (%, 625 um^2)	~0.05%		~0.05%	~0.038%	~0.031%
Defect Density (1/cm^2) (Vbd < 3.3V Failure)	> 1.0		> 0.3	< 0.05	

TABLE 3.1 Comparison of MIM performance for different bottom electrode materials

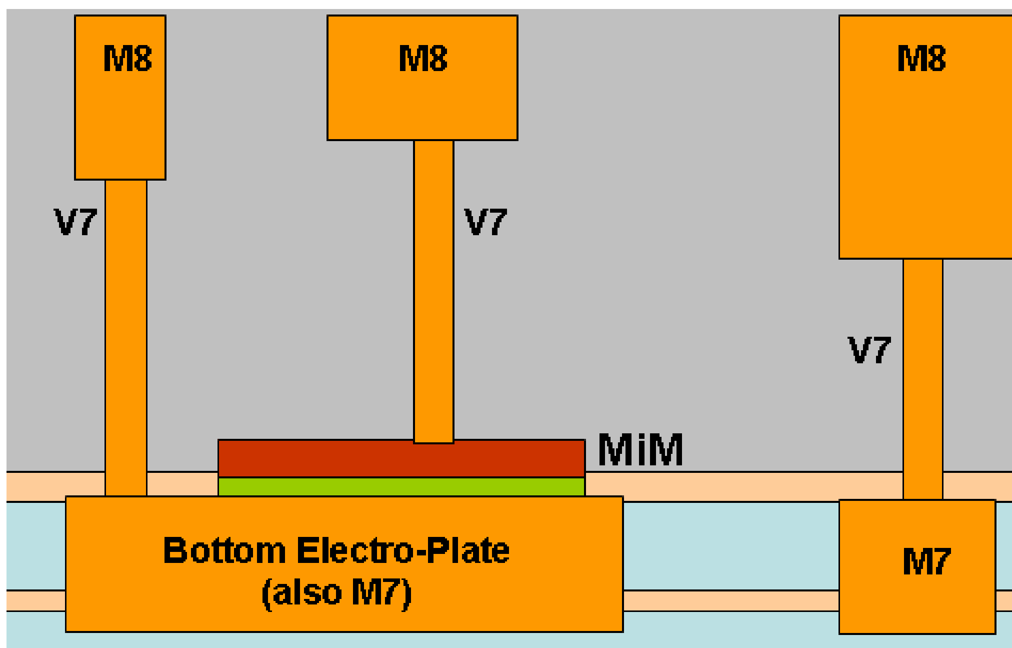

Fig. 3.1 Structure of MiM capacitor with Cu interconnect as bottom electro-plate

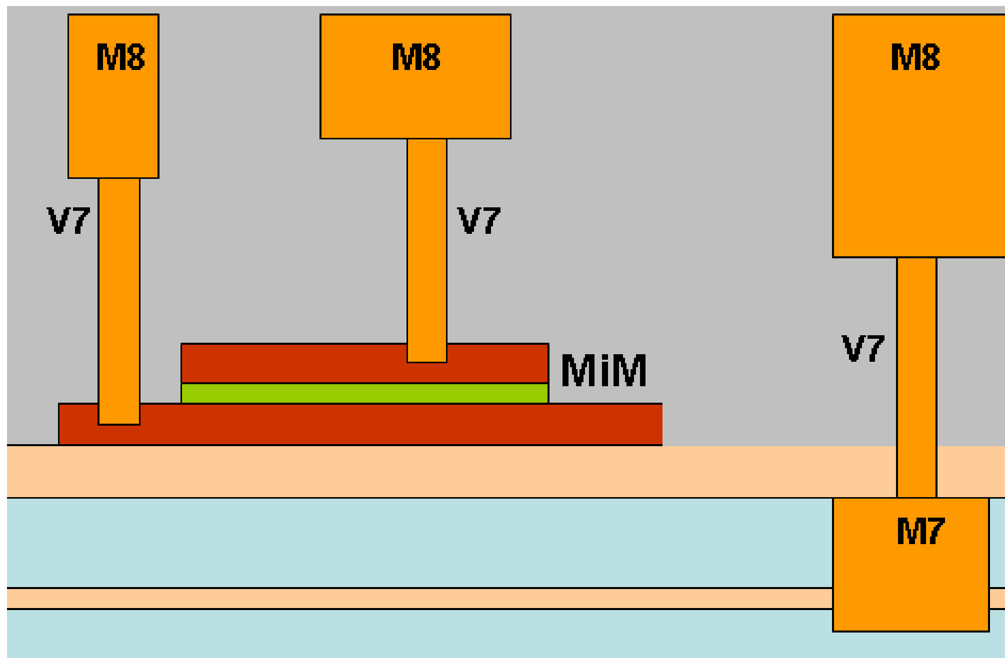

Fig. 3.2 Structure of MiM capacitor inserted between top two Cu layers

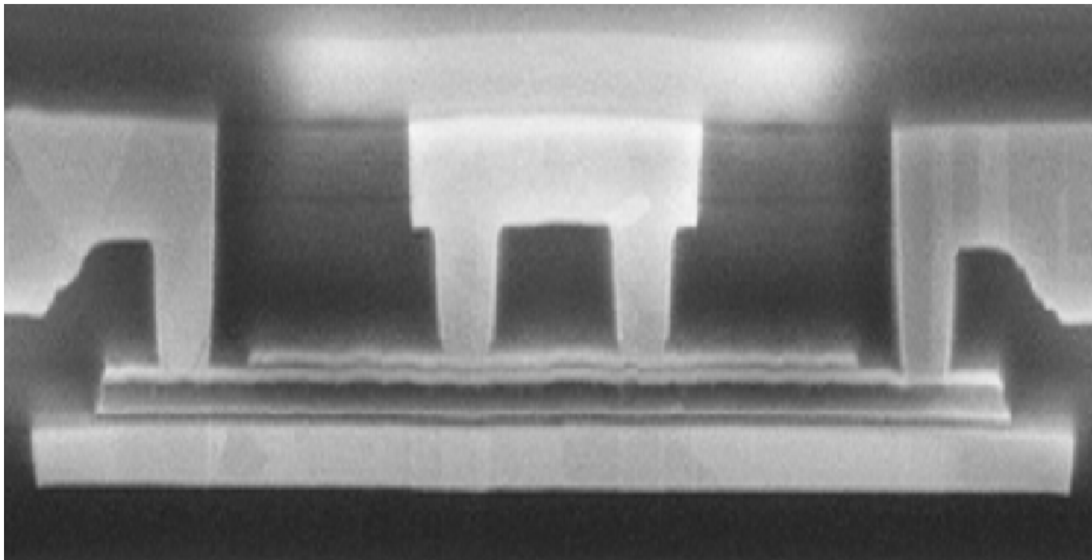

Fig. 3.3 TEM of integrated MiM capacitor with TaN/Al/TaN bottom electrode and TaN top electrode.

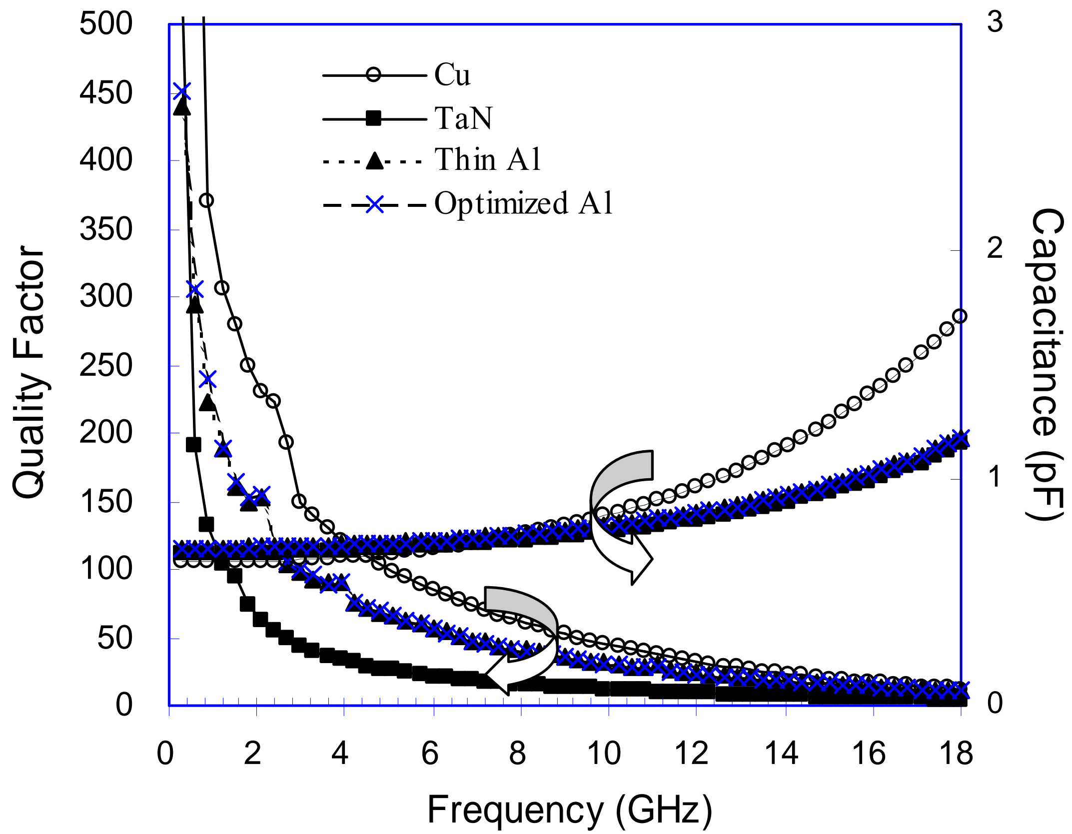

Fig. 3.4 The quality factor of 25 μm × 25 μm MIM capacitors. Cu has the highest quality factor with ~200 at 2.4GHz. TaN/Al/TaN showed Q~115 but TaN is only 54 at 2.4 GHz.

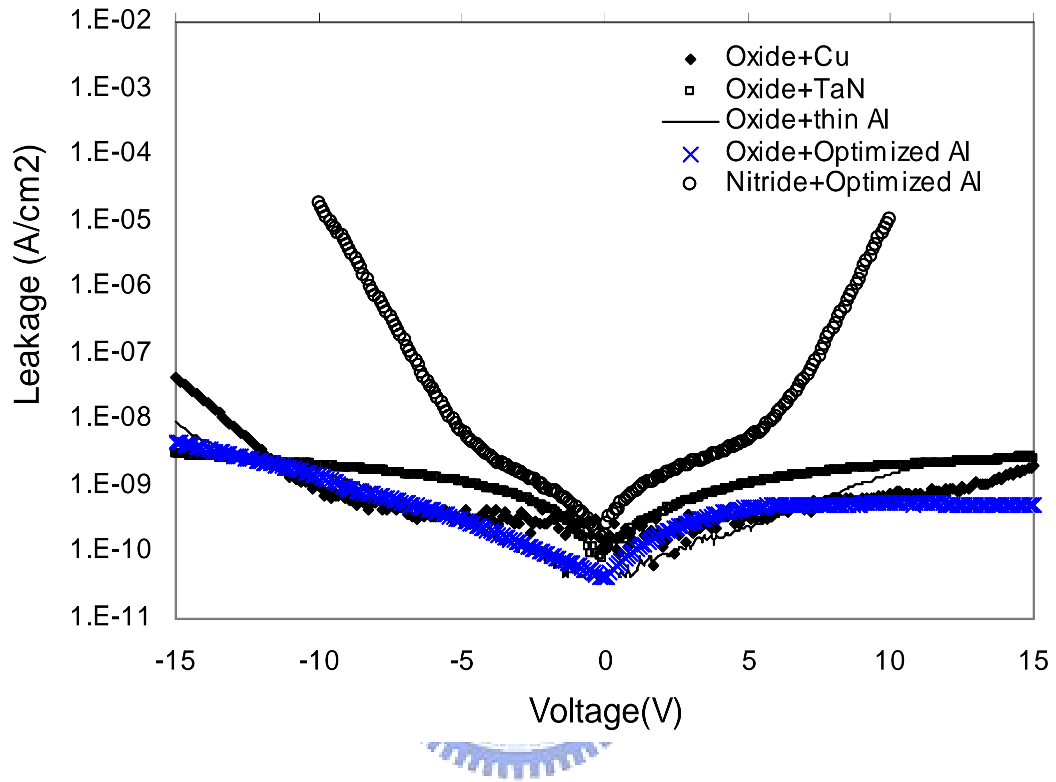

Fig. 3.5 Comparison of current vs. voltage behavior for different bottom electrode material.

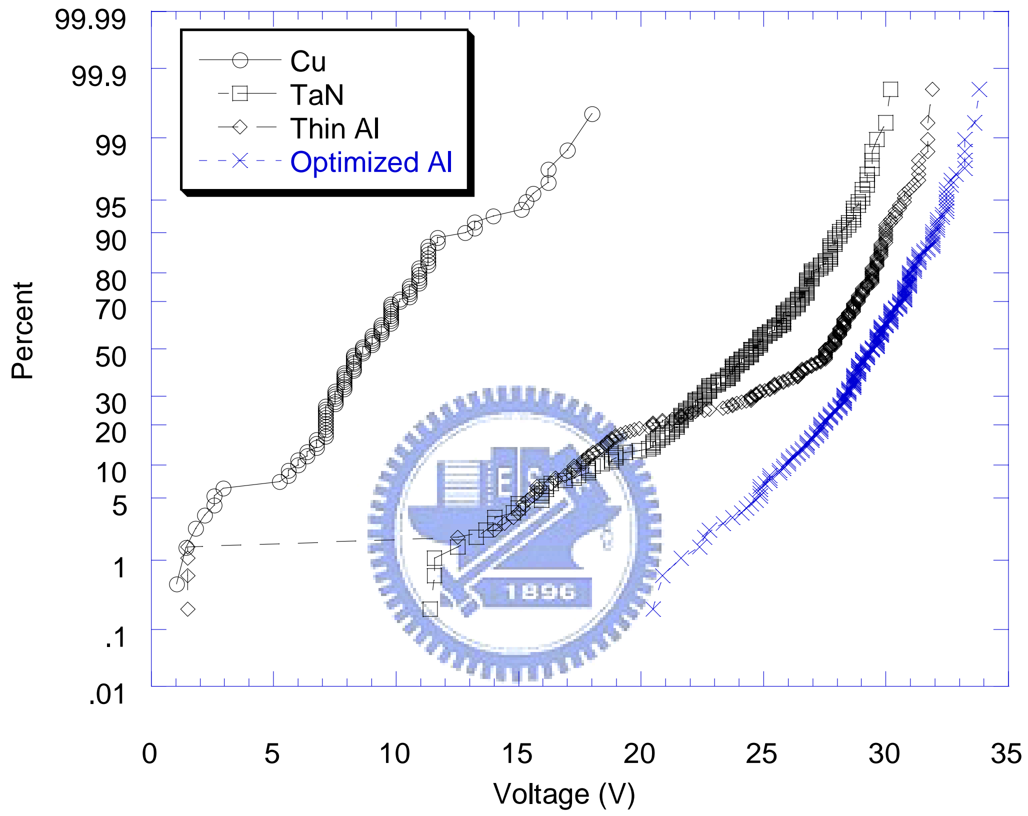

Fig. 3.6 MIM V_{bd} comparison with different bottom electrode-plates. Wafers with optimized TaN/Al/TaN bottom electrode showed best voltage breakdown performance.

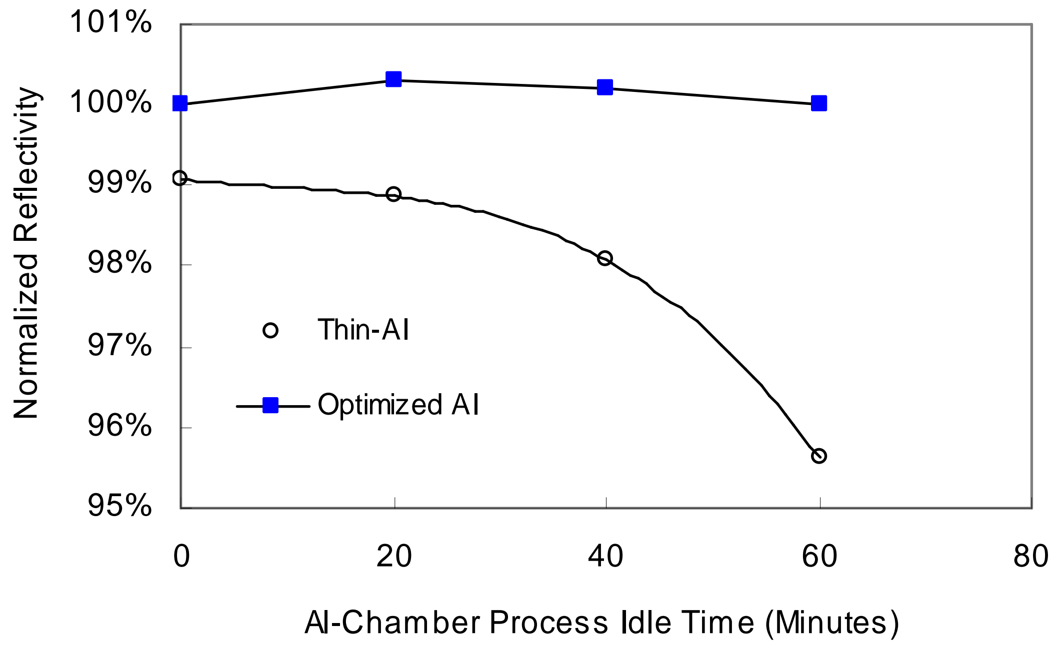

Fig. 3.7 Normalized Reflectivity vs. Al-deposition waiting time to show the relative surface

roughness effect.

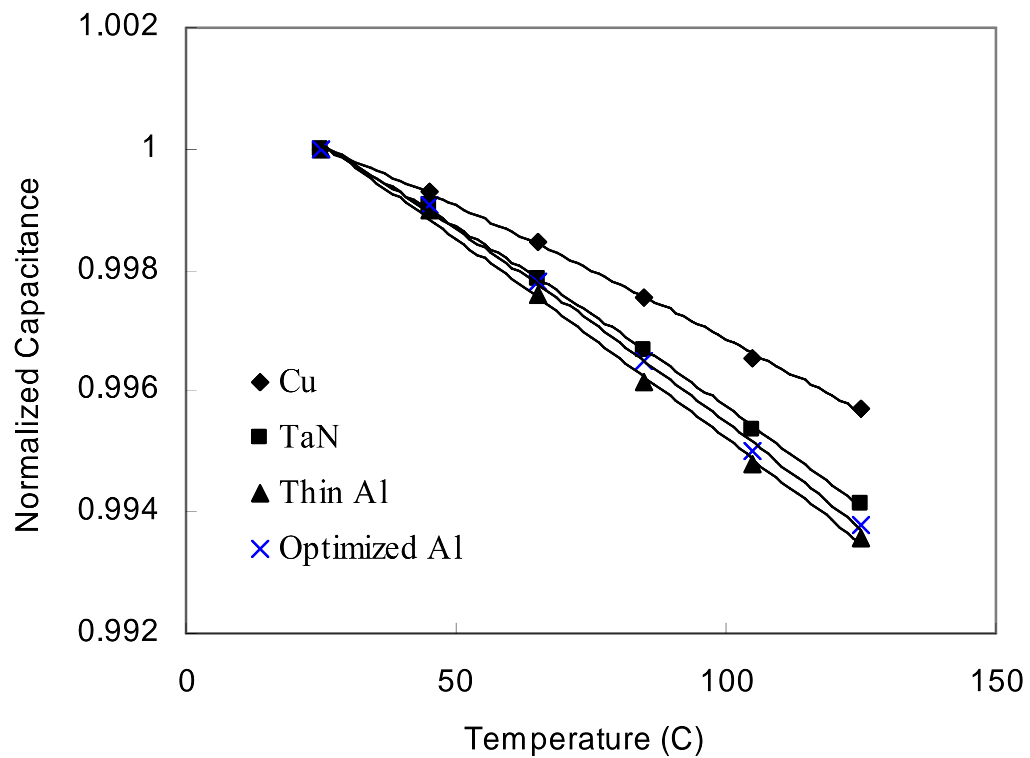

Fig. 3.8 Comparison of Temperature Linearity on MiM Capacitors. Cu bottom electro-plate

has the smallest TCC1 with –35 ppm/^{o}C.

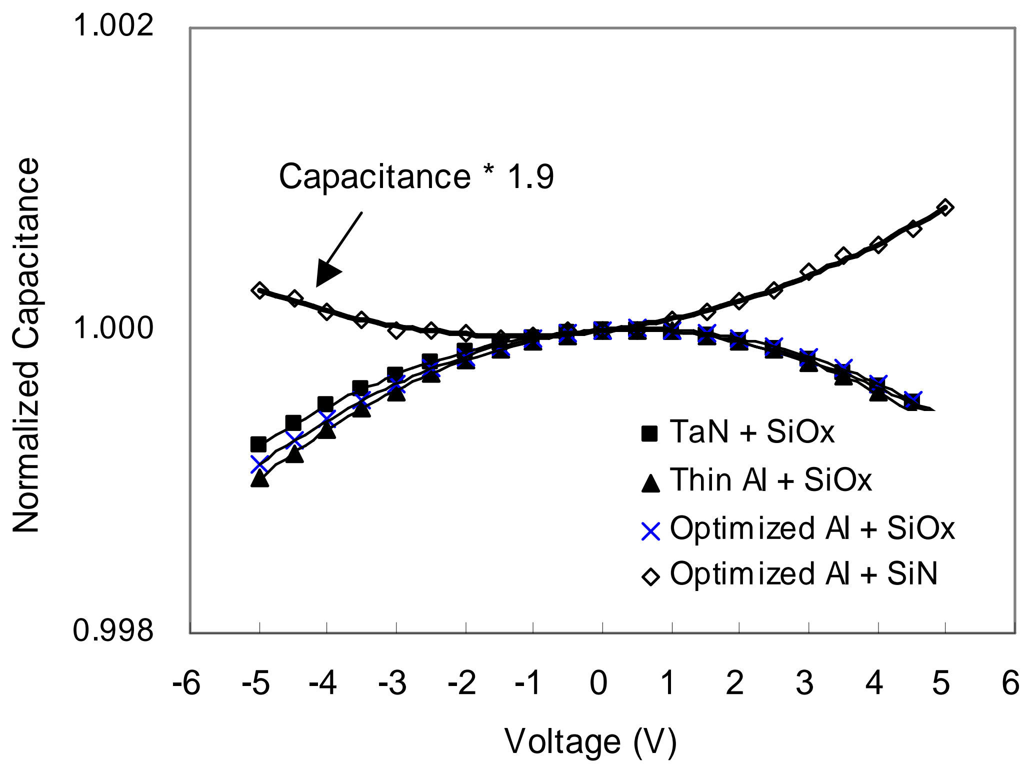

Fig. 3.9 Comparison of Voltage Linearity on MiM Capacitors. Nitride dielectric showed a positive VCC2 compared with negative VCC2 of SiO_2.

Chapter 4

Asymmetric-LDD MOS Transistor for SoC Design

The improvement of RF performance along with technology scaling has made CMOS the prime choice for RF-SoC design. However, the difficult part to realize a transceiver on a single chip is to integrate power amplifier. The low drain breakdown voltage of Si-MOS device is the most challenging issue to be resolved for RF-SoC design. Therefore, we have proposed a new device structure based on current Si-MOS process technology with 38% RF output power improvement at peak PAE by raised drain operation voltage.

4.1 CMOS is the Trend for MS/RF SoC Design

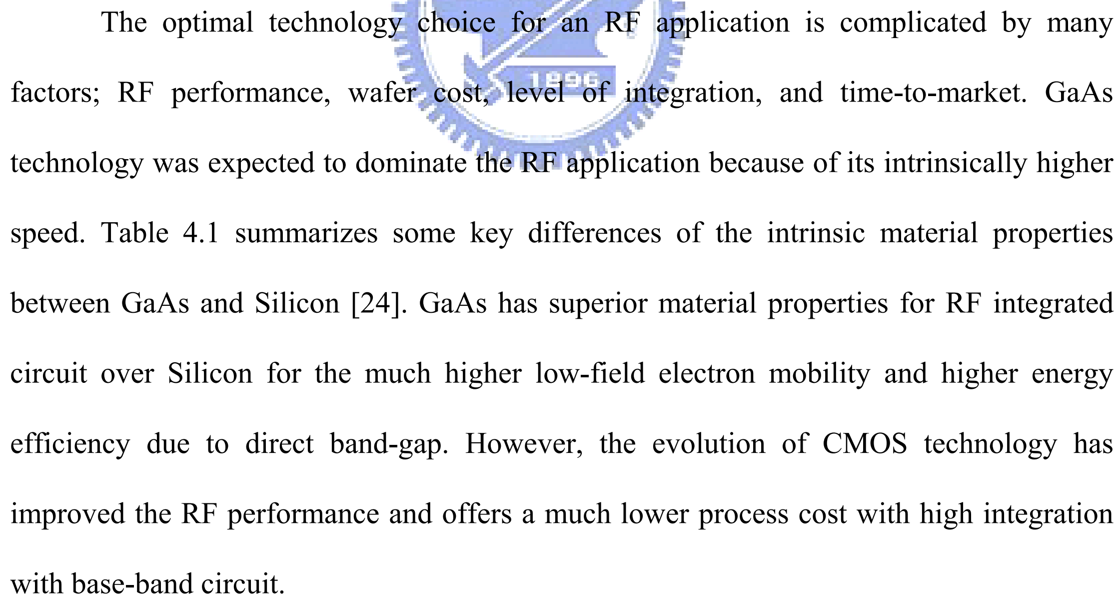

The optimal technology choice for an RF application is complicated by many factors; RF performance, wafer cost, level of integration, and time-to-market. GaAs technology was expected to dominate the RF application because of its intrinsically higher speed. Table 4.1 summarizes some key differences of the intrinsic material properties between GaAs and Silicon [24]. GaAs has superior material properties for RF integrated circuit over Silicon for the much higher low-field electron mobility and higher energy efficiency due to direct band-gap. However, the evolution of CMOS technology has improved the RF performance and offers a much lower process cost with high integration with base-band circuit.

The technology scaling of CMOS process evolves with shorter gate length, thinner gate oxide thickness, and lower operation voltage. Along with the improved device speed and reduced cost per transistor, the maximum oscillation frequency (f_{max}) is also improved larger than 50 GHz for 0.18 μm technology node [1]. At very short gate length (roughly

below 0.2 μm), the saturated drift velocity of the electrons dominates the cut-off frequency (f_t), and transistors fabricated in silicon and GaAs technologies have comparable cutoff frequencies, albeit at higher voltage levels with the silicon-based devices [25]. These technology improvements and cost reduction have made CMOS process the prime choice for Mixed-Signal and Radio-Frequency (MS/RF) SoC. However, the realization of high-power RF amplifier in 0.13 μm technology node is still a challenge due to the low breakdown voltage of thin gate oxide thickness and device punch-through in conventional MOSFETs. The limitation on breakdown voltage causes the low power gain in 0.13 μm technology and beyond. This has made the design of RF power amplifiers in 0.13 μm technology a difficult task.

Several device designs were introduced to improve the high-voltage breakdown of MOS transistors such as LDMOS [12]-[14] and Drain-extended MOS [26]. However, these devices are not suitable for RF SoC due to either low f_{max} or complicate process design. The most challenging effort is to design high-voltage MOS transistors by using the minimum gate length and core gate oxide thickness to gain the benefits of technology scaling. On the other hand, the added process cost should be minimized or none. Therefore, we have designed an asymmetric-LDD MOS transistor which can be further scaled. By enlarging the gate length, the drain breakdown voltage will be further improved according to the design requirements. The proposed asymmetric-LDD MOS transistor is suitable for MS/RF SoC design.

Even though Silicon-based technology has become the dominant technology for RF integrated circuit, GaAs (or InP)-based technologies will continue to maintain a small portion of RF applications because of higher low-field mobility which has a direct impact on device noise figure [27]. In some cases, even a few tenths of a decibel difference in noise figure is significant for wireless applications; especially in base station and satellite

receiver.

4.2 Device Design of Asymmetric-LDD MOSFET

Low noise amplifies (LNA) are one of the key active components in an RF system. Low noise and high linearity are required for LNA to content with a variety of signals coming from the antenna. Two measures of these requirements are the amplifier noise figure and the third-order input intercept point (IIP3); both determines the spur free dynamic range (SFDR). The SFDR determines the difference between the maximum detectable signal (MDS) and the maximum input signal prior to significant distortion [28]. In addition, high gain and low DC power consumption are other requirements of a LNA.

Power amplifiers (PA) for RF application must simultaneously satisfy requirements of gain, linearity, output power, and power-added efficiency. Along with technology evolution, the trend is to use lower power supply voltages. This makes it difficult to maintain the required output power and efficiency due to impedance matching limitations. Power amplifiers are typically operated in the Class-AB mode for most RFIC applications to achieve a compromise between power-added efficiency and linearity. The factors of key importance for amplifier performance are maximum oscillation frequency (for high power gain), linearity (for lowest possible adjacent channel interference), and breakdown voltage.

In conventional MOS transistor design, lightly-doped-drain (LDD) was introduced to reduce the high electric-field at the drain side and improve the drain breakdown voltage. However, this kind of MOS transistor design will provide a conducting path from drain to the gate edge. Higher drain voltage will cause either gate oxide breakdown or device punch-through under different gate voltages. To increase the operation voltage at the drain side, a N^+-P^- junction at the drain side is designed for NMOS

transistor to reduce the maximum voltage beneath the gate electrode.

The structure comparison of (a) the new asymmetric-LDD MOS transistor and (b) conventional MOS transistor are shown schematically in Fig. 4.1. Some different asymmetric LDD structures [29]-[32] were used to increase current drive capability with fully overlapped source implant. However, the fully overlapped source device has a worse hot carrier injection and does not have a high voltage capability. To increase the transistor breakdown voltage for RF power application, the LDD region at the drain side was removed, which is the major difference to a conventional MOS transistor. This was accomplished by blocking the ion implantations to LDD region and Halo process at the drain side for the new transistor. The devices we studied in this work are multiple finger MOS transistors with 10 gate fingers, 0.23 μm gate length and 5 μm width. For comparison, the same interconnect and RF layout were used [7]-[11]. The schematics of realizing asymmetric-LDD Si-MOS transistor is shown in Fig. 4.2. An extra layer was drawn to be excluded during Boolean operation while generating LDD masks.

The applied drain voltage will create a depletion region formed by drain to channel implant beneath spacer region. The depletion region will extend into the gate electrode while applying higher drain voltage. At the same time, higher electric field in the depletion region will have more voltage drop across the spacer region while applying higher drain voltage. The MEDICI simulated potential distribution of asymmetric-LDD NFET is shown in Fig. 4.3. The I_d-V_{ds} curves with various gate voltages for an asymmetric-LDD MOS with L_g=0.15 μm is also shown in Fig. 4.4.

The devices were fabricated by a standard logic process provided by IC foundry. The RF power characterization was carried out by on-wafer measurements at 2.4 GHz using an ATN load-pull system, where the input and output impedance matching conditions were selected to optimize the output power.

4.3 Drain Breakdown Voltage of Asymmetric-LDD MOSFET

Figure 4.5 shows the comparison of DC drain breakdown voltage for conventional and asymmetric-LDD MOS transistors. For the conventional MOS transistor, a BV_{dss} of 3.6 V was measured at I_{ds} of 0.1 μA/μm and V_{gs} of 0 V. However, the maximum drain bias is only 1.8 V if considering the reliability of 10 years continuous operation [7]. In sharp contrast, the BV_{dss} of the asymmetric-LDD transistor is increased to 7.0 V as measured under the same criteria. This large improvement of BV_{dss} is due to the designed wide depletion region beneath the spacer region and between the drain and substrate. In contrast, the existing n+-LDD in a conventional CMOS transistor just provides an electrically short path between inversion channel and drain. Such wide depletion region in the new design can support significantly larger reverse-biased drain voltage than conventional case. This new device design with large drain depletion region is similar to bipolar transistor from the device physics point-of-view. Since the electrons can pass through the drain depletion region with fast saturation velocity under large reverse biased voltage, little degradation of operation speed can be expected. Therefore, this new asymmetric-LDD MOS transistor can effectively resolve the fundamental challenge of low breakdown voltage issue in the small energy bandgap Si MOS transistor. In the meanwhile this device still preserves the high frequency operation of sub-μm MOS transistors with cutoff frequency (f_t) of 34 GHz close to the 35 GHz of conventional MOS. This device also gives a higher maximum oscillation frequency (f_{max}) of 86 GHz than the 76 GHz of conventional MOS. It is generally known the increasing breakdown voltage may lower down the drive current. However, the new asymmetric MOSFET can be operated at a higher voltage that gives close drive current (10.44 mA at V_{ds}=2.5 V) to conventional device (9.76 mA at V_{ds}=1.8 V). One major reliability issue for conventional deep sub-μm MOSFET is the Hot Carrier Injection (HCI)

degradation [33], caused by impact ionization and electrons injection into the gate oxide by high drain field. Device structure with LDD and spacer was introduced to reduce the peak electric field beneath the gate electrode that will cause serious hot carrier injection into gate dielectrics. From detailed transistor simulation T-Supreme Medici Analysis (TMA) [34], the asymmetric-LDD device design pushes the peak electric field away from the gate edge and reduces the electron injection into the gate oxide. Thus, good HCI reliability may be expected for this new device.

4.4 RF Power Performance of Asymmetric-LDD MOSFET

We have further measured the RF power performance in the asymmetric-LDD MOS transistor. The output power and PAE versus the input power of both the conventional and asymmetric-LDD MOS transistors are shown in Fig. 4.6. The DC bias point of the conventional MOS transistor is at V_{gs} of 1.2 V and V_{ds} of 1.8 V under the maximum trans-conductance condition. For the asymmetric-LDD MOS transistor, the DC bias point is at V_{gs} of 1.2 V and an increased V_{ds} of 2.5 V. Here only 2.5 V is chosen in this study although higher bias voltage can be used after detailed reliability study. The output power is increased by 38% from 130 to 180 mW/mm, as measured at 2.4 GHz under peak PAE condition. The PAE of asymmetric device at low input power is slightly lower than conventional device, which may be due to inferior electron transportation through the potential barrier at drain side. But this effect becomes less affective due to the electron tunneling via potential barrier at high electric field and bias voltage. In addition, broader maximum PAE region is also obtained in the asymmetric-LDD MOS transistor that provides wider design margin, in combination with the slightly increasing peak PAE from 23.5% to 24.9%. Moreover, when both devices are biased for 10 dBm output power measured at 2.4 GHz, the PAE can be improved by 16%. These achieved large

improvements of power performance are a new breakthrough in RF Si CMOS transistors and important for wireless communication IC and SoC. The dynamic load-lines of both (a) asymmetric-LDD Si-MOS transistor and (b) conventional Si-MOS transistor are shown in Fig. 4.7 to illustrate the improved RF performance due to the choice of operation point with raised drain voltage for asymmetric-LDD Si-MOS transistor.

The carrier to third-order inter-modulation product output power (C/IM3) ratio is another important factor for RF power application. We have compared the C/IM3 for the two MOS transistors and the results are shown in Fig. 4.8. The asymmetric-LDD MOS transistor still shows a slightly improved C/IM3 ratio of 0.7 dB at peak PAE. The improvement is due to the reduced gate-drain coupling capacitance (C_{gd}) by removing the LDD implant beneath the spacer; this reduces the interference between gate and drain nodes and therefore improves the linearity. Therefore, significantly better output power density is achieved by the asymmetric-LDD MOS transistor with even slightly better linearity and PAE. However, the drain resistance (R_{gd}) is also increased along with reduced C_{gd}, which causes an increased threshold voltage.

4.5 Summary

The low drain breakdown voltage of a conventional CMOS transistor is the major restriction of RF power performance. We have designed an asymmetric-LDD MOS transistor to increase the drain breakdown voltage from 3.6 V to 7.0 V. By raising the drain operation voltage beyond conventional CMOS device, the RF output power of this new transistor is improved by as much as 38% at peak PAE, with the added merit of broader peak PAE region and useful for wider design margin. By removing LDD at the drain side but keeping the spacer, an N^+-P^- depletion region is formed at the drain side. The thickness of this capacitive depletion region is significantly larger than conventional

symmetrical design, which allows larger voltage applied to drain. Thus, this drain engineering can improve the drain breakdown voltage and power performance. This new asymmetric-LDD MOS transistor is fully embedded in the standard CMOS logic process provided by foundries without any process modification.

Properties	Silicon	GaAs

Breakdown Field (V/cm)	~3x10^5	~4x10^5
Electron Mobility (cm^2/V-sec) at 300K	1500	8500
Energy Bandgap (eV) at 300K	1.12	1.424
Thermal Conductivity at 300K (watt/cm-^{o}C)	~1.45	~0.45
Saturated Electron Drift Velocity (@10^5 V/cm)	~10^7	~10^7
1/f Noise Corner Frequency (Hz) BJT/HBT MOSFET/MESFET	 10~10^3 10^3~10^5	 10^4~10^6 10^6~10^8
Substrate Resistivity (typical) (Ω-cm)	~10^3	~10^8
Dielectric Constant	11.9	13.1

Table 4.1 Comparison of fundamental material properties between Silicon and GaAs

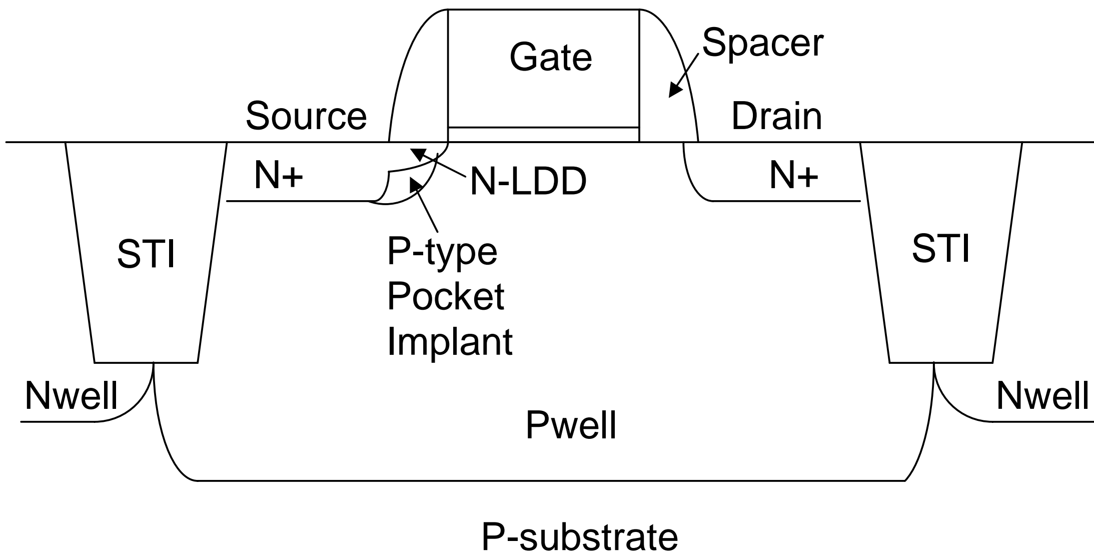

(a)

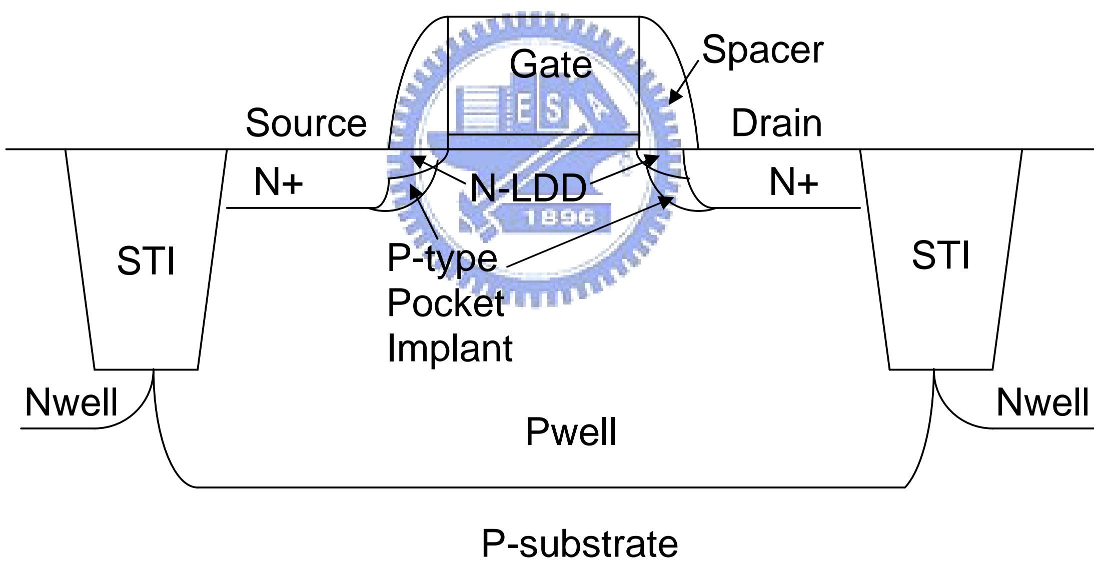

(b)

Fig. 4.1 Device structure of (a) an asymmetric-LDD MOS transistor and (b) a conventional MOS transistor.

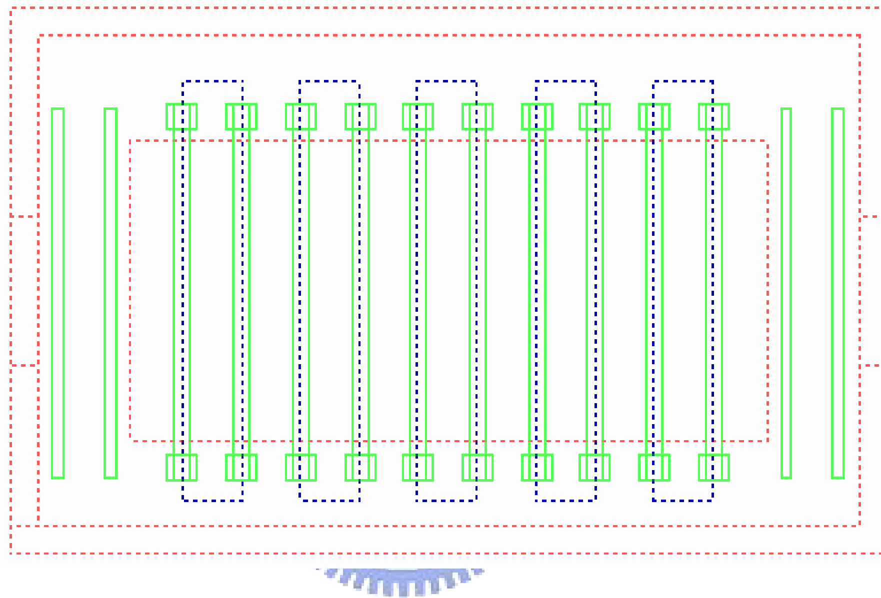

Fig. 4.2 Schematics of realizing asymmetric-LDD Si-MOS device with drawn layer at drain side of multi-finger MOSFET device structure.

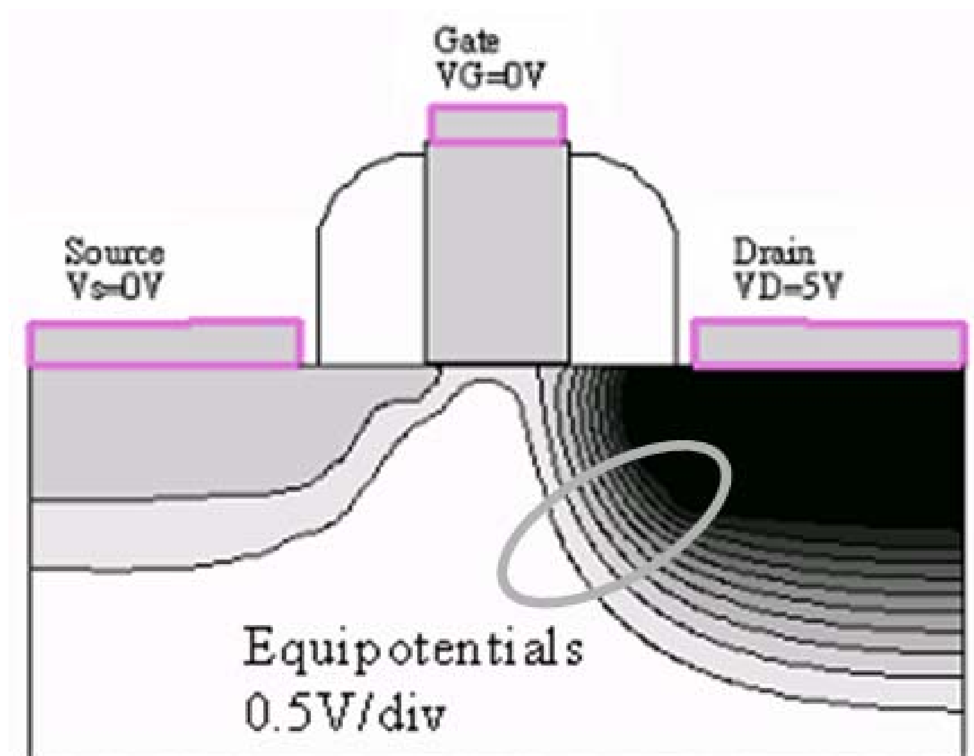

Fig. 4.3 MEDICI simulated potential distribution of asymmetric-LDD NFET.

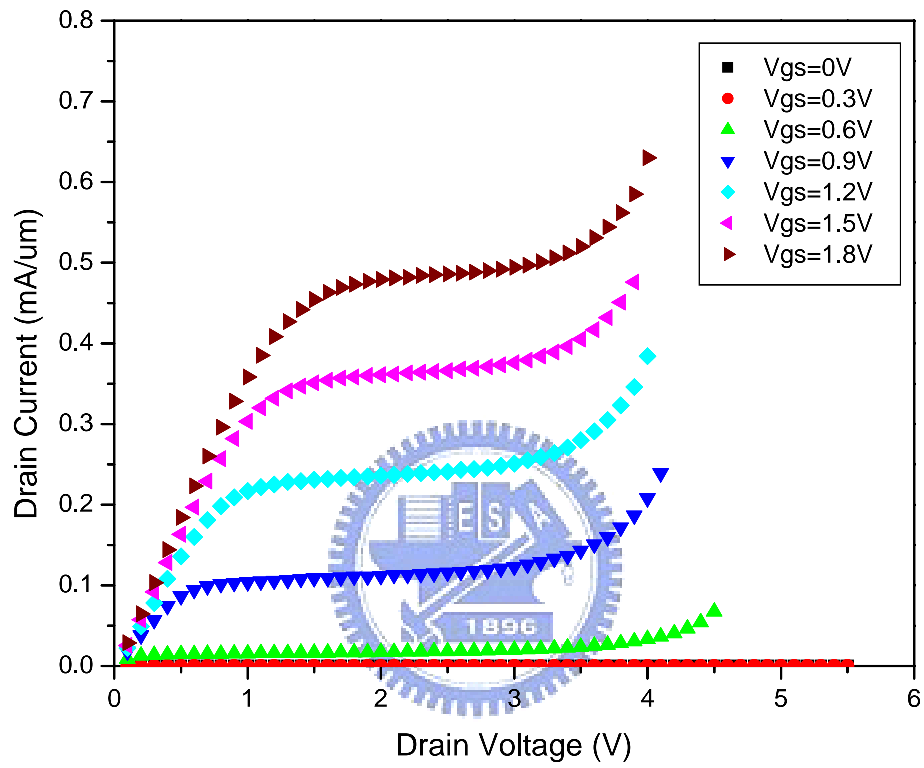

Fig. 4.4 I-V curves of asymmetric-LDD NMOS with Lg=0.15μm.

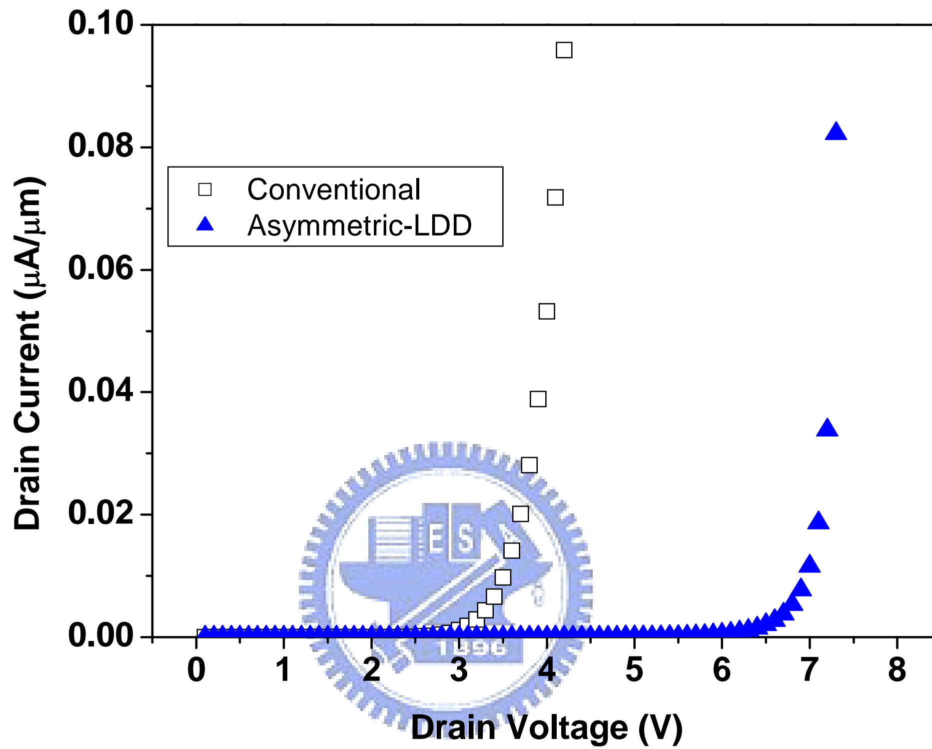

Fig. 4.5 Comparison of drain breakdown voltage (BV_{dss}) at Vgs=0V. The devices have a physical gate length of 0.23 μm. Significantly larger BV_{dss} is obtained using the new design.

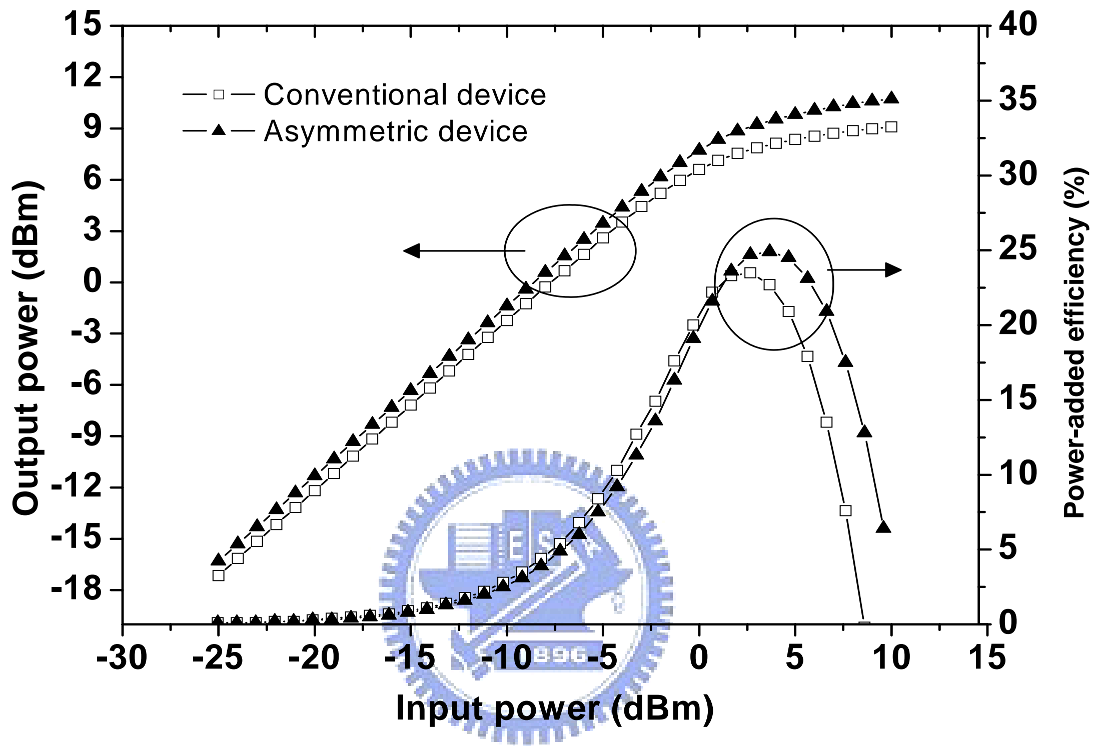

Fig. 4.6 Measured RF output power and PAE versus the input power for conventional and asymmetric-LDD MOS transistors at 2.4 GHz. Higher output power and broader PAE are measured for this new asymmetric-LDD MOS transistors.

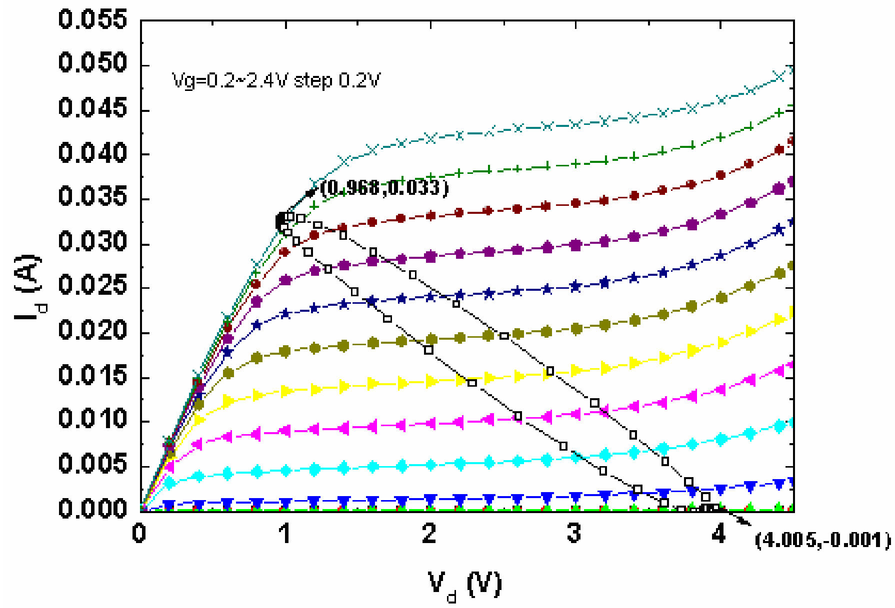

(a)

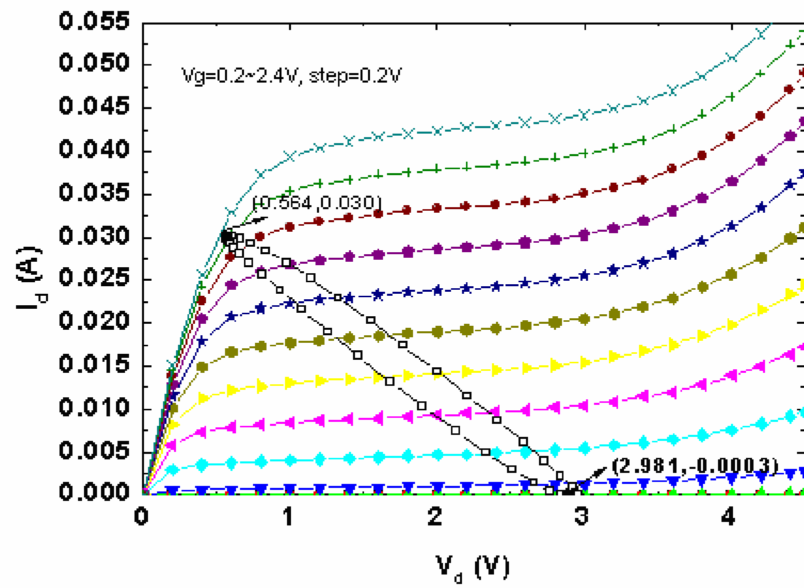

(b)

Fig. 4.7 Comparison of dynamic load-lines of (a) asymmetric-LDD Si-MOS transistor and (b) conventional Si-MOS transistor.

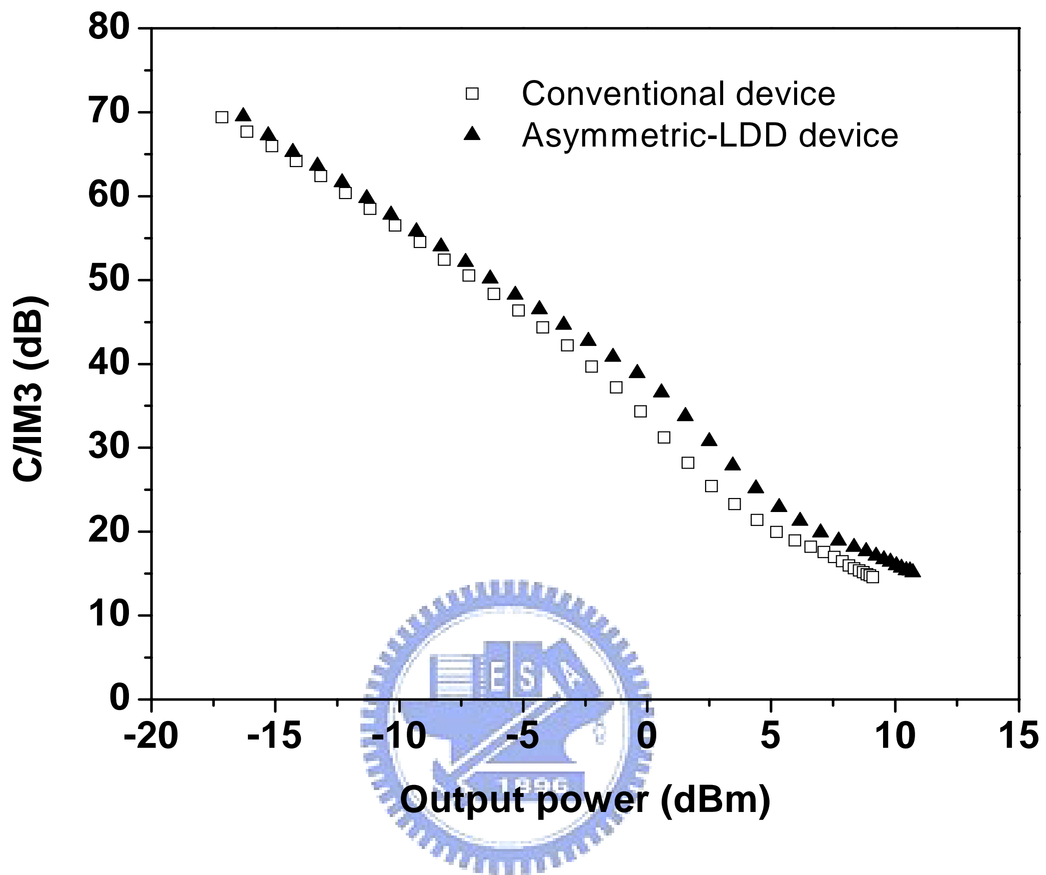

Fig. 4.8 Carrier to third-order inter-modulation product output power ratio (C/IM3) versus the output power for the two different devices measured at 2.4 GHz.

Chapter 5

Conclusion and Future Works

5.1 Conclusions

Wireless communication has become more and more important among various technologies that help people to communicate with each other and facilitate our daily life. Wireless communication has been realized and evolved with better quality, higher speed, and ease of usage. No matter the application is cellular wireless communication through Global System for Mobile Communications (GSM), Code Division Multiple Access (CDMA), or Wideband CDMA (WCDMA) or non-cellular communication through Wireless Local-Area Network (WLAN), Bluetooth, Wireless Personal Area Network (QPAN), or Ultra Wide-Band (UWB), wireless has shortened the distance between people and ease our daily life. RF circuits realized by CMOS technology are also playing a more important role in wireless communication as CMOS technology keeps evolving. The much improved RF performance has made RF-CMOS the prime choice for Mixed-Signal/RF SoC design.

In this dissertation, two key components for Mixed-Signal/RF design were discussed; one is MiM capacitor and the other is RF-CMOS device. We have also discussed how to optimize the RF performance by properly select finger number and finger width and how to extract the intrinsic RF noise. The process design consideration of implementing MiM capacitor into Cu BEOL process was discussed. Different methods of implementing MiM capacitor into Cu BEOL were proposed and the performance was compared. MiM capacitors with Cu as bottom electro-plat achieved higher Q-factor compared with MiM capacitor with either TaN or TaN/AlCu/TaN as bottom electro-plat due to much lower resistance. However, the

V_{bd} cumulative failure of Cu electrode-plate is much worse than TaN and TaN/Al/TaN electrodes due to worse surface roughness and inevitable Cu-CMP u-scratch. To balance the performance and reliability requirements, the proposed MiM structure is to insert MiM capacitor between the top two Cu layers with TaN/AlCu/TaN as the bottom electro-plate.

For high-Q and small MiM area product, Cu as a capacitor bottom plate is a suitable option but has a lower process yield. TaN-based MiM capacitor achieved low leakage and better linearity but a penalty of low quality factor ~54 @2.4GHz due to higher resistivity. On the other way, a MiM capacitor with thin Al bottom plate had been achieved with optimized process condition. The Al-base MiM capacitor achieved Q>100 at 2.4GHz with ~0.7pF capacitance. The optimized process conditions also achieved a very low defect density and suitable for manufacturing. The process design and performance comparison of integrating different MiM structures into Cu damascene process was discussed.

A new asymmetric-LDD MOS device was proposed to improve the drain-breakdown voltage but keeping the high-speed performance along with technology evolution. The designed asymmetric-LDD MOS transistor demonstrated the increase of drain breakdown voltage from 3.6 V to 7.0 V. By raising the drain operation voltage beyond conventional CMOS device, the RF output power of this new transistor was improved by as much as 38% at peak PAE, with the added merit of broader peak PAE region and useful for wider design margin. This new asymmetric-LDD MOS transistor is also fully embedded in the standard CMOS logic process provided by foundries without any process modification

5.2 Future Works

The new asymmetric-LDD transistor has demonstrated better RF performance compared with conventional CMOS devices. Our future work is to implement this new device into an RF power amplifier and improve the power performance that is a critical part for Mixed-Signal/RF SoC design.